Metsähovi Radio Observatory

# Multifrequency connection in blazars: Tool for studying the location and emission mechanisms

Venkatessh Ramakrishnan

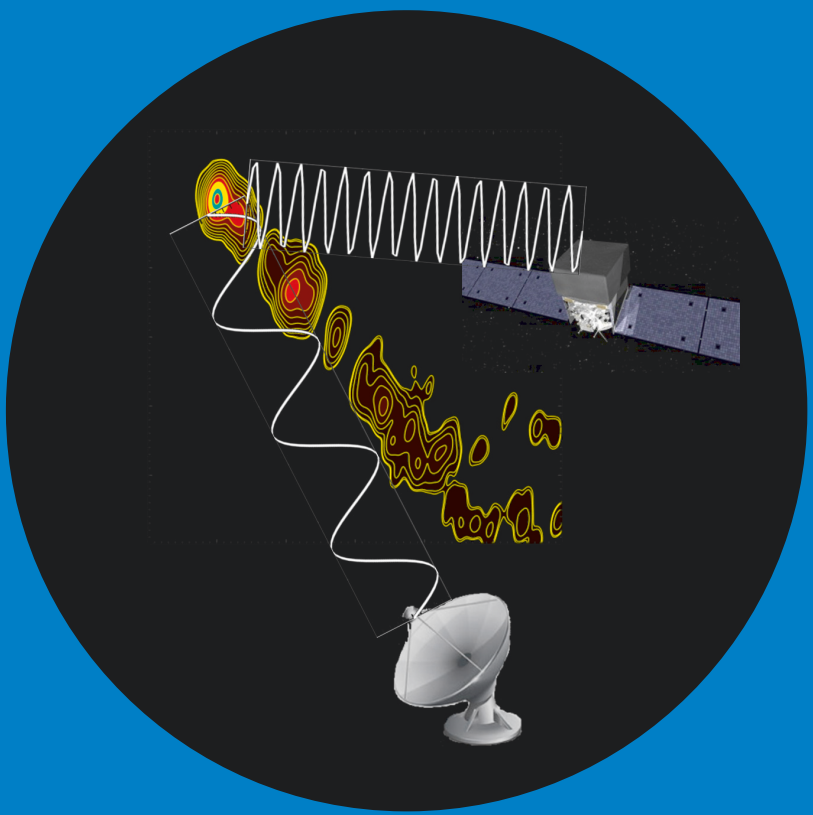

Aalto University

DOCTORAL DISSERTATIONS

Aalto University publication series
**DOCTORAL DISSERTATIONS** 47/2016

# Multifrequency connection in blazars: Tool for studying the location and emission mechanisms

**Venkatessh Ramakrishnan**

A doctoral dissertation completed for the degree of Doctor of Science (Technology) to be defended, with the permission of the Aalto University School of Electrical Engineering, at a public examination held at the lecture hall AS1 of the TUAS building on 22 April 2016 at 12.

**Aalto University**
**School of Electrical Engineering**
**Metsähovi Radio Observatory**

**Supervising professor**
Professor Anne Lähteenmäki

**Thesis advisor**
Docent Merja Tornikoski

**Preliminary examiners**
Professor Matthias Kadler, Institut für Theoretische Physik und Astrophysik, Universität Würzburg, Germany
Doctor Stefan Larsson, Institutionen för astronomi, Stockholms universitet, Sweden

**Opponent**
Professor Stefan Wagner, Landessternwarte Königstuhl, Universität Heidelberg, Germany

Aalto University publication series
**DOCTORAL DISSERTATIONS** 47/2016



ISBN 978-952-60-6704-9 (printed)
ISBN 978-952-60-6705-6 (pdf)
ISSN-L 1799-4934
ISSN 1799-4934 (printed)
ISSN 1799-4942 (pdf)
http://urn.fi/URN:ISBN:978-952-60-6705-6

Unigrafia Oy
Helsinki 2016

Finland

Aalto University

# Abstract

Aalto University, P.O. Box 11000, FI-00076 Aalto www.aalto.fi

**Author**
Venkatessh Ramakrishnan

**Name of the doctoral dissertation**
Multifrequency connection in blazars: Tool for studying the location and emission mechanisms

**Publisher** School of Electrical Engineering

**Unit** Metsähovi Radio Observatory

**Series** Aalto University publication series DOCTORAL DISSERTATIONS 47/2016

**Field of research** Space Science and Technology

**Manuscript submitted** 19 November 2015 **Date of the defence** 22 April 2016

**Permission to publish granted (date)** 18 February 2016 **Language** English

☐ **Monograph** ☒ **Article dissertation** ☐ **Essay dissertation**

**Abstract**

Blazars are a sub-class of AGN with relativistic jets oriented towards the line of sight of the observer. The radiation mechanism in the radio, and sometimes in optical and X-rays, are dominated by synchrotron processes with high-energy emission arising from the inverse-Compton scattering of photons by the relativistic electrons or through hadronic processes. The latter scenario is one of the topics debated in the blazar research, primarily owing to the location of the seed photons for the high-energy emission. This problem is contemplated in this thesis for a sample of blazars. A proper understanding of the physical mechanisms responsible for variability is contingent upon a mathematical and statistical description of the phenomena. Hence, the variability of all light curves was investigated using power spectral density and Bayesian blocks, and its connection using the discrete correlation function.

The connection between the variability at 37 GHz and gamma-ray light curves was studied in 55 blazars. The average time delay from this study showed that the variations in the radio lagged behind those at gamma rays. However, by taking the size of the radio core into account the gamma-ray emission region was localised to the radio core in the majority of sources. In another work, the cross-correlations were performed for 15 blazars using light curves at 37 GHz, 95 GHz, R-band and gamma rays. Due to the shorter time span of the light curves and undersampled optical data in some cases, significant correlations were obtained only in a few sources. The variations at 37 GHz and 95 GHz were simultaneous in most of the sources, indicating that the opacity constraints at both these frequencies were similar.

The connection between the events in the radio through gamma rays was studied in the blazars 1156+295, Mrk 421 and OJ 248. From the correspondence of the activity at both radio and gamma rays in 1156+295, and also based on the ejection time of the shocks from the Very Long Baseline Array analysis, a causal connection constraining the gamma-ray flares to the parsec-scale radio jet is established. The physical explanation for the radio variability in Mrk 421 is discussed by modelling the radio and gamma-ray light curve under a one-zone SSC framework. For OJ 248, a multifrequency connection for the 2012 gamma-ray flare is explored using cross-correlations.

To understand the synchrotron processes, the radio spectra of 104 AGN from *Planck* satellite observations are analysed. The shape of most of the spectra is consistent with those predicted by the shock-in-jet model. The overall conclusion from this thesis is that in most of the blazars studied the gamma-ray emission arises from the parsec-scale radio jet, which supports the SSC mechanism (through one- or multi-zone models) for the high-energy emission.

**Keywords** AGN; emission - radio, optical, gamma rays; time series - PSD, cross-correlation

**ISBN (printed)** 978-952-60-6704-9 **ISBN (pdf)** 978-952-60-6705-6

**ISSN-L** 1799-4934 **ISSN (printed)** 1799-4934 **ISSN (pdf)** 1799-4942

**Location of publisher** Helsinki **Location of printing** Helsinki **Year** 2016

**Pages** 231 **urn** http://urn.fi/URN:ISBN:978-952-60-6705-6

# Preface

I am very much indebted for the enduring support provided by my advisor, Docent Merja Tornikoski. She has been instrumental in moulding my work, and by honing my areas of interest for a better future. The encouragement from my supervisor, Professor Anne Lähteenmäki has been reassuring throughout this journey.

The guidance of Talvikki during these years has been valuable. Her insights into my work helped to prove their significance and to organise my insatiable curiosity to a better level. I also regard Jonathan's and Liza's guidance with utmost importance during the first two years. Thanks to Elina Nieppola, Joni and Tuomas for the interesting discussions on various topics related to astronomy.

Special thanks to Ari and Juha Aatrokoski for the best technical support I could ever get. Thanks for bestowing upon me *The Ultimate Force (TUF)*. I am grateful to Eki and Henkka for helping with the purchase of my car and in its repair during the mid-winter season. Thanks to all other members of Metsähovi for various light-hearted moments. I thank my friends Emilia and Lotta for possessing the tenacity and be of assistance during numerous occasions.

I also acknowledge the support of all the staffs at Tuorla Observatory, with special thanks to Kari and Elina Lindfors. Thanks to Esko for his ideas and support over the past four years. The guidance and perseverance of Kaj in the field of radio astronomy and instrumentation will be useful throughout my career. Thanks for the support during my stay in Finland, particularly for your determination that motivated me to pursue doctoral research at this reputed facility.

I am extending my gratitude to Professor Alan Marscher and Doctor Svetlana Jorstad for sharing their knowledge and continuing their collaboration since my second year. The contour plot of 3C 273 on the cover

image is credited to their VLBA programme. I am also grateful to William Martin for reviewing the language of this manuscript.

Finally, I thank my family for their support and confidence that allowed me to accept the fortuitous opportunity of attaining the master's and doctoral degree in Finland.

I acknowledge the support from the Finnish Graduate School of Astronomy and Space Physics. This work has made use of the computational resources provided by the Aalto Science-IT project.

Espoo, March 13, 2016,

Venkatessh Ramakrishnan

# Contents

# List of Publications

This thesis consists of an overview and of the following publications which are referred to in the text by their Roman numerals.

**I** **Venkatessh Ramakrishnan**, Jonathan León-Tavares, Elizaveta A. Rastorgueva-Foi, Kaj Wiik, Svetlana G. Jorstad, Alan P. Marscher, Merja Tornikoski, Iván Agudo, Anne Lähteenmäki, Esko Valtaoja, Margo F. Aller, Dmitry A. Blinov, Carolina Casadio, Natalia V. Efimova, Mark A. Gurwell, José L. Gómez, Vladimir A. Hagen-Thorn, Manasvita Joshi, Emilia Järvelä, Tatiana S. Konstantinova, Evgenia N. Kopatskaya, Valeri M. Larionov, Elena G. Larionova, Liudmilla V. Larionova, Niko Lavonen, Nicholas R. MacDonald, Ian M. McHardy, Sol N. Molina, Daria A. Morozova, Elina Nieppola, Joni Tammi, Brian W. Taylor and Ivan S. Troitsky. The connection between the parsec-scale radio jet and $\gamma$-ray flares in the blazar 1156+295. *Monthly Notices of the Royal Astronomical Society*, 445, 1636–1646, October 2014.

**II** **V. Ramakrishnan**, T. Hovatta, E. Nieppola, M. Tornikoski, A. Lähteenmäki and E. Valtaoja. Locating the $\gamma$-ray emission site in *Fermi* /LAT blazars from correlation analysis between 37 GHz radio and $\gamma$-ray light curves. *Monthly Notices of the Royal Astronomical Society*, 452, 1280–1294, August 2015.

**III** **V. Ramakrishnan**, T. Hovatta, M. Tornikoski, K. Nilsson, E. Lindfors, M. Baloković, A. Lähteenmäki, R. Reinthal and L. Takalo. Locating the $\gamma$-ray emission site in *Fermi* /LAT blazars. II Multifrequency correlations. *Monthly Notices of the Royal Astronomical Society*, 456, 171–180, January 2016.

**IV** *Planck* Collaboration: P. A. R. Ade, N. Aghanim, H. D. Aller, ..., **V. Ramakrishnan**, + 44 co-authors. *Planck* Intermediate Results.

Radio spectra of northern extragalactic radio sources. *Astronomy & Astrophysics*, 2015 submitted.

**V** T. Hovatta, M. Petropoulou, J. L. Richards, D. Giannios, K. Wiik, M. Baloković, A. Lähteenmäki, B. Lott, W. Max-Moerbeck, **V. Ramakrishnan** and A. C. S. Readhead. A combined radio and GeV $\gamma$-ray view of the 2012 and 2013 flares of Mrk 421. *Monthly Notices of the Royal Astronomical Society*, 448, 3121–3131, January 2015.

**VI** M. I. Carnerero, C. M. Raiteri, M. Villata, J. A. Acosta-Pulido, F. D'Ammando, P. S. Smith, V. M. Larionov, I. Agudo, M. J. Arévalo, A. A. Arkharov, U. Bach, R. Bachev, E. Benítez, D. A. Blinov, V. Bozhilov, C. S. Buemi, A. Bueno Bueno, D. Carosati, C. Casadio, W. P. Chen, G. Damljanovic, A. Di Paola, N. V. Efimova, Sh. A. Ehgamberdiev, M. Giroletti, J. L. Gómez, P. A. González-Morales, A. B. Grinon-Marin, T. S. Grishina, M. A. Gurwell, D. Hiriart, H. Y. Hsiao, S. Ibryamov, S. G. Jorstad, M. Joshi, E. N. Kopatskaya, O. M. Kurtanidze, S. O. Kurtanidze, A. Lähteenmäki, E. G. Larionova, L. V. Larionova, C. Lázaro, P. Leto, C. S. Lin, H. C. Lin, A. I. Manilla-Robles, A. P. Marscher, I. M. McHardy, Y. Metodieva, D. O. Mirzaqulov, A. A. Mokrushina, S. N. Molina, D. A. Morozova, M. G. Nikolashvili, M. Orienti, E. Ovcharov, N. Panwar, A. Pastor Yabar, I. Puerto Giménez, **V. Ramakrishnan**, G. M. Richter, M. Rossini, L. A. Sigua, A. Strigachev, B. Taylor, M. Tornikoski, C. Trigilio, Yu. V. Troitskaya, I. S. Troitsky, G. Umana, A. Valcheva, S. Velasco, O. Vince, A. E. Wehrle and H. Wiesemeyer. Multiwavelength behaviour of the blazar OJ 248 from radio to $\gamma$-rays. *Monthly Notices of the Royal Astronomical Society*, 2677, 450–464, May 2015.

# Author's Contribution

**Publication I: "The connection between the parsec-scale radio jet and $\gamma$-ray flares in the blazar 1156+295"**

In this work, a detailed study of the blazar 1156+295 is undertaken using 43 GHz Very Long Baseline Array observations coupled with the multifrequency observations from radio through $\gamma$-ray bands. The author performed the $\gamma$-ray and VLBA data analysis, and other statistical tests discussed in the work. The author was also responsible for writing the paper.

**Publication II: "Locating the $\gamma$-ray emission site in *Fermi* /LAT blazars from correlation analysis between 37 GHz radio and $\gamma$-ray light curves"**

In this work, a detailed analyses on the variability through Power Spectral Density, cross-correlation and Bayesian block analysis was carried out by the author. The author reduced the $\gamma$-ray data required for this work and was involved in 37 GHz observations. Following this, the author interpreted the results from all the analyses, and took the responsibility of writing the paper.

**Publication III: "Locating the $\gamma$-ray emission site in *Fermi* /LAT blazars. II Multifrequency correlations"**

The author performed the $\gamma$-ray data reduction and 37 GHz observations, and analysed the multifrequency data of the sources. The results from the statistical tests performed in the work were interpreted and written

for the paper by the author.

### Publication IV: "*Planck* Intermediate Results. Radio spectra of northern extragalactic radio sources"

The author modelled the radio spectra of the sources using broken power-law and was also involved in the interpretation and compilation of the work.

### Publication V: "A combined radio and GeV $\gamma$-ray view of the 2012 and 2013 flares of Mrk 421"

The author analysed the Power Spectral Density and cross-correlations of radio and $\gamma$-ray data of the source.

### Publication VI: "Multiwavelength behaviour of the blazar OJ 248 from radio to $\gamma$-rays"

Besides observing the source at 37 GHz, the author also made contributions to the cross-correlation analysis discussed in the work.

# List of Figures

# List of Abbreviations

| | |
|---|---|
| AGN | Active Galactic Nuclei |
| BLO | BL Lacertae Object |
| BLR | Broad-Line Region |
| CARMA | Combined Array for Research in Millimeter-wave Astronomy |
| DCF | Discrete Correlation Function |
| DFT | Discrete Fourier Transform |
| EIC | External Inverse-Compton |
| EGRET | Energetic Gamma-Ray Experiment Telescope |
| FSRQ | Flat Spectrum Radio Quasar |
| HFI | High Frequency Instrument |
| HSP | High Synchrotron Peaked |
| ICS | Inverse Compton scattering |
| ISP | Intermediate Synchrotron Peaked |
| LAT | Large Area Telescope |
| LFI | Low Frequency Instrument |
| LSP | Low Synchrotron Peaked |
| NLR | Narrow-Line Region |
| PDF | Probability Density Function |
| PSD | Power Spectral Density |
| RBL | Radio-selected BL Lacertae Object |

| | |
|---|---|
| SED | Spectral Energy Distribution |
| SMA | Sub Millimeter Array |
| SMBH | Supermassive Black Hole |
| SSC | Synchrotron Self-Compton |
| VLBI | Very Long Baseline Interferometry |
| XBL | X-ray-selected BL Lacertae Object |

# List of Symbols

| | |
|---|---|
| $B$ | Magnetic field density |
| $c$ | Speed of light (= 2.997 $\times 10^{8}$ m s$^{-1}$) |
| $D_{\rm L}$ | Luminosity distance |
| $e$ | Charge of an electron (= 1.602 $\times 10^{-19}$ coulombs) |
| K | Kelvin |
| $k$ | Boltzmann constant (= 1.380 $\times 10^{-23}$ erg K$^{-1}$) |
| $L_{\rm EIC}$ | Luminosity of EIC process |
| $L_{\rm synch}$ | Luminosity of synchrotron process |
| $L_{\rm SSC}$ | Luminosity of SSC process |
| $L_{\odot}$ | Luminosity of the sun (= 3.846 $\times 10^{33}$ erg s$^{-1}$) |
| $M_{\odot}$ | Mass of the sun (= 1.989 $\times 10^{30}$ kg) |
| $m_e$ | Mass of an electron (= 9.109 $\times 10^{-31}$ kg) |
| $S_{\nu}$ | Flux density |
| $T_{\rm b}$ | Brightness temperature |
| $t_{\rm var}$ | Variability time-scale |
| $U_B$ | Energy density of the magnetic field |
| $U_{\rm ph}$ | Energy density of the target photon field |
| $z$ | Redshift |
| Å | Angstrom (= $10^{-10}$ m) |

| | |
|---|---|
| $\alpha$ | Spectral index |
| $\alpha_{\rm mm}$ | Spectral index at millimetre wavelengths |
| $\alpha_{\rm sub-mm}$ | Spectral index at sub-millimetre wavelengths |
| $\alpha_X$ | X-ray spectral index |
| $\beta_{\rm app}$ | Apparent speed |
| $\Gamma$ | Lorentz factor |
| $\gamma$ | Electron Lorentz factor |
| $\delta$ | Doppler factor |
| $\theta$ | Viewing angle |
| $\nu_{\rm break}$ | Break frequency |
| $\nu_g$ | Gyrofrequency of electron |
| $\nu_s$ | Synchrotron frequency of elctron |
| $\nu_{\rm syn}^{\rm pk}$ | Synchrotron peak frequency |
| $\sigma_{\rm T}$ | Thomson cross section |
| $\tau$ | Time delay |
| $\phi$ | Opening angle |
| $\chi^2_{\rm dist}$ | Goodness of fit statistic |

# 1. Active Galactic Nuclei

## 1.1 Introduction

The central region of massive galaxies releases a substantial amount of energy that is capable of outshining an entire host galaxy. These are called active galactic nuclei (AGN). Their classification based on disparate criteria ranges from Seyfert galaxies ($10^7\ L_\odot$) to quasars ($10^{15}\ L_\odot$) and hence is not necessarily mutually exclusive. It is to be noted that not all galaxies have an active nucleus. In the early twentieth century, photometric and spectroscopic observations detected many nebulae with distinct emission lines (Fath 1909; Slipher 1917). The extragalactic origin of these objects was established through the works of Hubble (1926) and Seyfert (1943). Despite these early optical observations, the initial understanding about the energetic output from AGN came with the advent of radio astronomy (Reber 1944), which are more dominant non-thermal emitters.

Radio astronomy began with the works of Karl Jansky in 1932 with the discovery of the following sources: local and distant thunderstorms, and the static using rotatable antenna at a wavelength of 14.6 m. The static was later concluded to be of an extraterrestrial origin and was identified to come from the Milky Way (Jansky 1933). This discovery was soon followed by the detection of emissions from the Sun, the centre of the Milky Way (Sagittarius) and one in the constellation of Cygnus by Grote Reber (Reber 1944). In 1951, the extragalactic nature of the source was realised with the positional determination of the radio source Cygnus A using the Cambridge interferometer (Smith 1951). This was later followed by the identification of sources 3C 295 (Minkowski 1960), 3C 48 (Greenstein 1963) and 3C 273 (Schmidt 1963). An optical counterpart of a blue

star and a 'faint wisp' or 'jet' was identified by Maarten Schmidt and Bev Oke for the latter source (Schmidt 1963). Spectral studies of the 'star' however revealed broad emission lines consistent with known transitions at a redshift of $\sim$0.158, placing it well outside the galaxy. The 'star-like' appearance of these objects gives them their names, Quasi-Stellar Objects (QSOs) and Quasi-Stellar Radio Sources (quasars) for the radio-quiet and radio-loud sources, respectively.

### 1.2 The AGN paradigm

Despite all efforts to understand the AGN morphology in the early twentieth century, the one that gained importance was that of the accretion dominated process by a central massive object in a galaxy. This proposition was due to the immense radiation from 3C 273 ($10^{14}$ $L_{\odot}$), that can only be caused by such processes. In the following years, the presence of a black hole got established after several observational detections (e.g. Balick & Brown 1974; Brown & Lo 1982; Lea et al. 1982). The supermassive black holes with masses $\sim 10^5$–$10^{10} M_{\odot}$ are now considered to be present in every galaxy, including our own. These elusive objects evolve by engulfing the circumnuclear material through the process of accretion. After losing the potential energy, the accretion disc formed from the infalling matter thermally radiates due to viscosity. The accretion disc radiates mainly at optical to soft X-ray energies, and its temperature decreases with the increase in the mass of the black hole. Thus, the temperature of the accretion discs around stellar-mass black holes is approximately three orders of magnitude higher than those around supermassive black holes (Belloni 2010).

The spectroscopic observations in the 1970s revealed the presence of time variable emission lines in the AGN spectra. Some of the lines had Doppler widths in the range $10^3$–$10^4$ km s$^{-1}$ while others were a few hundred km s$^{-1}$. Based on the widths, they were categorised as Broad-Line Region (BLR) and Narrow-Line Region (NLR), respectively. The BLR contains the permitted emission lines, such as the hydrogen Balmer line series and are extensively studied by the reverberation mapping technique (e.g. Peterson 2008). Based on the photoionisation models, the temperature of the BLR is expected to be around $10^4$ K with a number density $\gtrsim 10^9$ cm$^{-3}$. The broad line width and the high temperature places the BLR within the potential well of the black hole ($\leq 1$ pc). Hence, firm con-

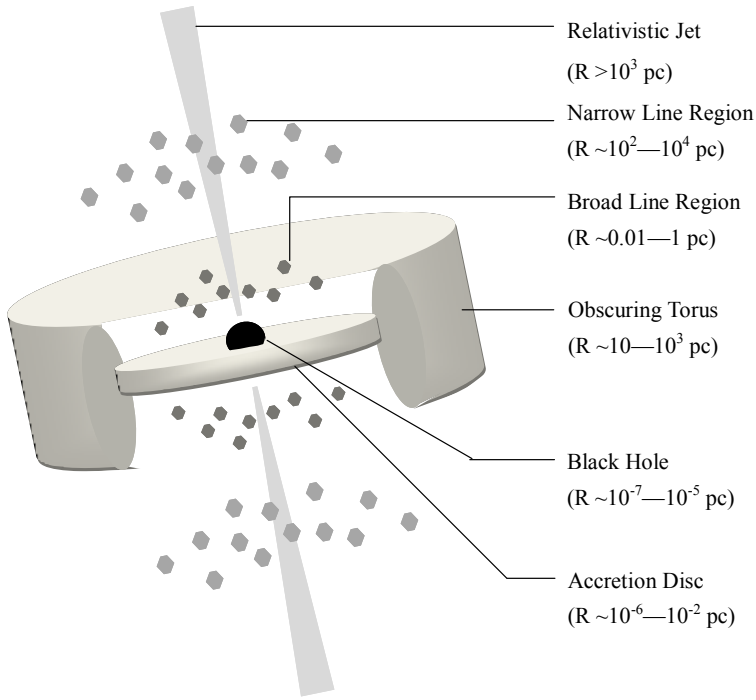


**Figure 1.1.** Generic structure of AGN. The AGN morphology is detailed here along with the approximate size of each region. This figure is after Urry & Padovani (1995).

straints on the physical properties of the supermassive black hole can be placed based on regular monitoring of the BLR in AGN. The NLR is characterised by (semi-) forbidden lines that show little variability. Their gas temperature ranges from 10000–25000 K with densities of $10^3$–$10^5$ cm$^{-3}$. The spatial scale of the NLR is understood to extend up to a kiloparsec mainly from the lack of variability and narrow line width. In recent years, the study of the NLR has provided insights into the binary supermassive black holes formed through galaxy mergers (e.g. Shen et al. 2011).

The dense molecular cloud that surrounds the black hole and accretion disc, while extending to hundreds of parsecs is called the torus. The torus is optically thick and re-radiate the dust and gas from the central regions in infrared and optical regimes. The visibility of the central region of an AGN depends on the orientation of the torus. Those AGN with a face on view of the torus show the BLR and the accretion disc in great detail (classified as Seyfert type 1); others obscure the central region (classified

as Seyfert type 2).

Another remarkable morphology of an AGN that was discovered in 1918 in the elliptical galaxy M87 (Curtis 1918) were a pair of relativistic jets. These are plasma structures that are energetic and highly collimated and are launched from the accretion disc. The jets propagate to kiloparsecs or more in distance.

The highly luminous jets are only observed in about 10 per cent of the AGN. These objects are classified as radio-loud AGN. Objects with very weak jets are called the radio-quiet AGN. The distinction between these two classes is mostly based on the spectral slope between the radio and optical band with the demarcation at 0.35 (della Ceca et al. 1994). Sources above this limit are radio-loud while those below are radio-quiet AGN. The orientation of relativistic jets in radio-loud AGN has led the way to the foundation of a unification scheme based on viewing angle. This model is to explain the different properties such as radio structures, brightness enhancement in jet due to shocks and levels of variability, observed in these objects (e.g. Antonucci 1993; Urry & Padovani 1995). Those AGN with the line of sight of the jet directed towards the observer are classified as blazars; the explanation for the enhancement in the emission of radio-loud AGN is discussed in Section 1.3.2. The schematics of the structure of AGN is shown in Figure 1.1.

## 1.3 Relativistic Jets

The first extensive model for explaining the processes powering the jet was postulated by Blandford & Znajek (1977). According to this model, jets are formed from the interaction of the ionised material with the magnetic field lines around the accretion disc that are twisted by the spinning black hole. This process, in turn, launches a jet on either side of the accretion disc. Following this model, Blandford & Königl (1979) proposed a model for interpreting the observations of relativistic jets.

The basic geometry of the jet is shown in Figure 1.2. The base of the visible portion of the jet at radio frequencies is assumed at a location $R_0$. The constant opening angle of the jet is $\phi$ and the angle it subtends to the line of sight of the observer is $\theta$. According to the model of Blandford & Znajek (1977), disturbances produced in the central engine pervade outward, which forms a shock on reaching the location $R_0$, since this region has a higher density of electrons and magnetic field strength. Processes such

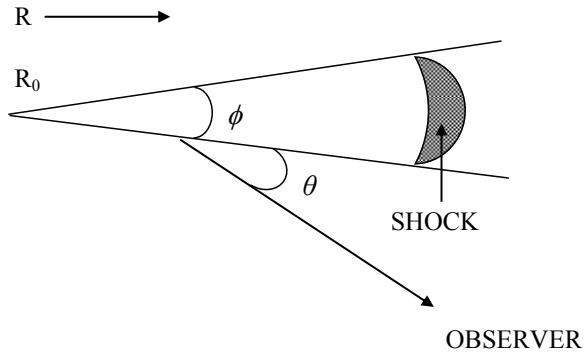


**Figure 1.2.** Geometry of relativistic jet model.

as the acceleration, collimation and energisation of the jet occur at distances of $R < R_0$. Hence probing the location $R_0$ can provide information regarding the connection between the jet and central engine.

The nonthermal emission due to the synchrotron radiation of the jet is detectable across the electromagnetic spectrum. Jets can be extensively studied in the radio frequencies using the technique of Very Long Baseline Interferometry (VLBI) with the capability to probe into the inner regions of the jet. The interferometric observations have revealed the structure of the jet to be short or long with curvature, along with the evidence of moving components that are either superluminal or subluminal, and sometimes even stationary (e.g. Lister et al. 2013).

### 1.3.1 Variability

The variability in radio-loud AGN is considered to be dominated by the emission from the relativistic jet. As mentioned above, the disturbances in the central engine causes the shocks to propagate down the jet. This claim was the emergence for the shock-in-jet model that shows shocks can reproduce the observed structural and spectral variability in flux density (e.g. Marscher & Gear 1985; Hughes et al. 1985, 1989). According to this model, flares start at the optical-infrared frequencies and lose their energy by Compton, synchrotron and adiabatic mechanisms.

According to the current AGN paradigm, the emission in radio to optical (and sometimes also X-rays) corresponds to synchrotron radiation from the jet. We mostly observe a time delay between the flare at higher and lower frequencies, as explained by the generalised shock model (Valtaoja et al. 1992a). They are a result of the relativistic electrons being accelerated along a shock front while losing energy by synchrotron pro-

cess. There are various techniques to characterise the time-scale and amplitude of variability in AGN, such as the Power Spectral Density (PSD), cross- and autocorrelation functions (CCF and ACF) and the structure function (see Section 3). These variables also relate to the size and structure of the emitting region.

### 1.3.2 Relativistic beamed emission

The apparent propagation of AGN jet components at speeds greater than that of the speed of light ($c$), was first proposed by the relativistic beaming model of Rees (1966), years before the VLBI observations came into practise. This apparent speed, $\beta_{\rm app}$, was understood as an optical illusion caused by the plasma moving at relativistic speeds, known as *superluminal motion*, which depends on the line of sight of the relativistic jet. To understand this, consider the propagation of a blob at speed $\beta$ (= $\nu/c$) along the line of sight $\theta$ as shown in Figure 1.2. The blob emits a radiation in the time interval $\Delta t_0$ in the observer's frame; in the source frame this reduces to $\Delta t_e = \Delta t_0/(1+z)$. The distance travelled by the blob in the observer's frame is given by $\nu \Delta t_e \cos\theta$ while the time interval is $\Delta t_0 = \Delta t_e(1-\beta\cos\theta)$. Based on the relation of transerve velocity, $\nu_{\rm app} = \beta_{\rm app} c$, with the true velocity, $\nu$ and $\theta$, the apparent speed in the plane of the sky reduces to (Pearson & Zensus 1987),

$$\beta_{\rm app} = \frac{\beta \sin\theta}{1-\beta\cos\theta}. \tag{1.1}$$

The apparent speed is maximum at $\theta = \sin^{-1}(1/\Gamma)$, where $\Gamma = (1-\beta^2)^{-1/2}$ is the Lorentz factor. This implies that a high Lorentz factor can be realised when the emission from the jet is beamed toward the observer.

The relativistic motion of the blob when directed toward the observer is strongly Doppler boosted causing an increase in the flux level. The activity begins to fade when the angle divulges from the observer. The Doppler boosting factor is given by

$$\delta = [\Gamma(1-\beta\cos\theta)]^{-1}. \tag{1.2}$$

From equations (1.1) and (1.2), $\Gamma$ and $\theta$ are related as

$$\Gamma = \frac{\beta_{\rm app}^2 + \delta^2 + 1}{2\delta} \tag{1.3}$$

and

$$\theta = \frac{2\beta_{\rm app}}{\beta_{\rm app}^2 + \delta^2 - 1}. \tag{1.4}$$

Due to Doppler boosting, the emission is significantly amplified, which in the case of blazars, is higher by an order of magnitude or more than other radio-loud AGN (e.g. Lähteenmäki & Valtaoja 1999; Hovatta et al. 2009). The variability time-scales are also affected by time dilation effects causing the time-scale in the observer's frame to be shorter than in the rest frame of the jet.

The variation in the particle density, magnetic field or jet diameter can be understood by estimating the brightness temperature ($T_{\rm b}$) gradient along the jet. The equation to estimate $T_{\rm b}$ is given by (Kadler et al. 2004)

$$T_{\rm b} = 1.22 \times 10^{12}{\rm K} \left(\frac{S_\nu}{\rm Jy}\right) \left(\frac{\nu}{\rm GHz}\right)^{-2} \left(\frac{d}{\rm mas}\right)^{-2} (1+z), \qquad (1.5)$$

where $S_\nu$ is the flux density, $\nu$ the frequency and $d$ is the angular size. For a stable conical jet geometry the particle density, magnetic field and the jet diameter is assumed to evolve with a power-law dependence on the distance from the base of the jet.

### 1.3.3 Kinematics of the Jet

The study of radio-loud AGN using VLBI has become popular ever since the first measurements in 1967. Since then, it has been shown that jets are relativistic on parsec (e.g. Lister et al. 2013) and kiloparsec scales (e.g. Biretta et al. 1995). The VLBI observations of radio-loud AGN have revealed the presence of a bright emission features that is located at a distance greater than 0.2 pc from the base of the jet (Pushkarev et al. 2012). These bright structures in AGN jets are mostly a stationary feature (Marscher 1995) that is termed as a standing shock (aka the *core*; $R_0$ in Figure 1.2). The core is marginally resolved or unresolved in VLBI images and is considered the origin of the jet in radio frequencies. Under the assumption that the core is located in a region with an optical depth of one, it is understood that its absolute position varies with frequency. This frequency-dependent position of the core is called the core-shift (see Figure 1.3; Lobanov 1998). The core-shift studies are based on the assumption of a conical jet, which in turn yields the magnetic field configuration and also the distance to the actual base of the jet (O'Sullivan & Gabuzda 2009; Pushkarev et al. 2012).

The shocks thus formed in a region closer to the supermassive black hole propagate down the jet. Apart from the core, numerous moving emission features are observed in VLBI images that are often found propagating beyond the core (e.g. Jorstad et al. 2005). These features upon emerg-

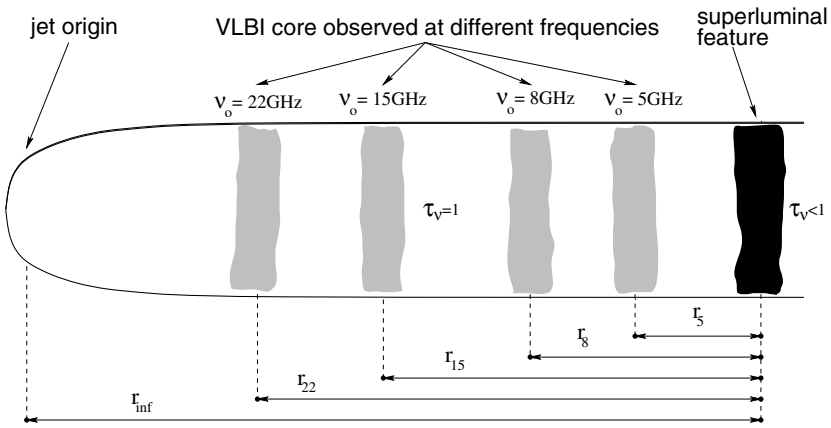


**Figure 1.3.** An illustration of frequency-dependent core-shift. Credit: Kovalev et al. (2008).

ing from the core radiate energy via different mechanisms depending on their energy while the radius of the jet undergoes an expansion. In certain cases, it is suggested that the expansion of the jet is followed by a re-collimation when the jet radius decreases and establishes as a shock, commonly referred to as the re-collimation shock. This phase leads to an increase in the pressure, density and magnetic field of this region. The moving feature then interacts with the re-collimation shock that is followed by an enhanced activity in the total flux-density light curves. The physical scenario is similar to that observed in the core of the jet; the propagation of the moving shock causes an increase in the jet radius. Therefore, the evolution of the moving feature beyond the re-collimation shock reconciles with the shock-in-jet model (Daly & Marscher 1988). Recent advances in VLBI observations have shown the presence of re-collimation shocks in AGN at distances less than a milli-arcsec (e.g. 3C 120 S1: León-Tavares et al. 2010, BL Lac: Cohen et al. 2014a) and also greater than 50 milli-arcsec (e.g. 3C 120 C80: Agudo et al. 2012, M87: Cheung et al. 2007) from the core.

Studies based on the hydrodynamical (HD) simulations have categorised the moving features into *forward/reverse structures* and *trailing shocks*. According to the HD simulations by (Aloy et al. 2003), when the relativistic jet is perturbed at its injection point, the disturbance propagates downstream, spreading asymmetrically along the jet, and finally splitting into two regions. Both of these regions contain enhanced energy densities with respect to the underlying jet, and thus the synchrotron flux rises. The leading forward shock and trailing reverse shock have higher and

lower Lorentz factors, respectively, than the underlying jet flow.

Another HD simulation finds that the interaction of the external medium with a strong shock pinches the surface of the jet, leading to the production of the trailing features (Agudo et al. 2001). These trailing shocks appear to be released in the wake of the primary moving shock rather than ejected from the core. Hence, a single strong component ejection from the jet nozzle may lead to the production of multiple emission features through this mechanism.

The alternate models to those involving shocks consider plasmoids propagating down the jets as discrete density enhancements called "blobs". These blobs traverse the jet expanding both longitudinally and laterally. Despite the argument for blobs, the shock scenario gained more importance as they are a viable model that could explain the dynamics of the jets, such as those discussed above.

## 1.4 Spectral energy distribution

In order to understand the physical processes in an AGN, the continuum radiation properties are to be fully probed. This is done with the construction of spectral energy distribution (SED) which can be characterised using various radiation models to understand the physics of the emission at the particular frequency. The shape of a SED also differs in various types of AGN. For example, the radio component of the SED peaks higher in radio-loud AGN than in their radio-quiet counterpart (e.g. Elvis et al. 1994). This thesis work has focussed solely on blazars which are radio-loud AGN. The SED of a blazar shows two prominent peaks (see Figure 1.4) with the low-frequency peak around the radio/infrared regime due to synchrotron radiation and the high-frequency peak in the $\gamma$-ray energies due to inverse-Compton or hadronic processes.

## 1.5 Blazars

Radio-loud AGN with relativistic jets oriented close to the line of sight of the observer are called blazars. The average viewing angle of blazars is 5° (Lister et al. 2013). Blazars account for less than five per cent of all AGN. The jet emission in these objects are Doppler boosted thus making it highly variable across the electromagnetic spectrum, from radio to

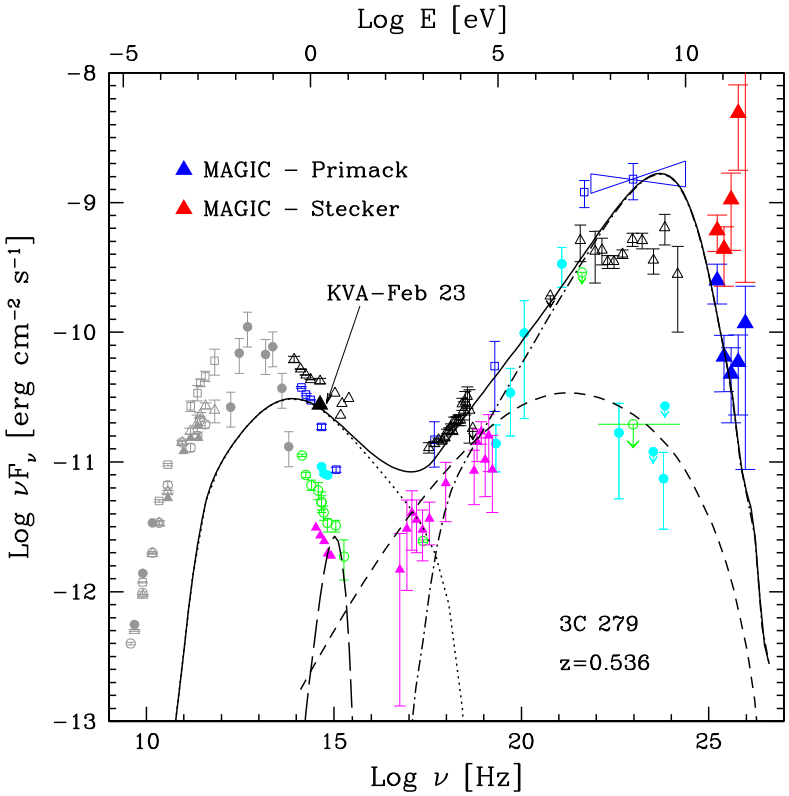


**Figure 1.4.** Spectral energy distribution for 3C 279 at different source intensities, over the years from 1991 to 2003, taken from Errando et al. (2008). The solid line represents the total model emission. The individual components of the emission model are synchrotron radiation (dotted line), accretion disc emission (long-dashed), synchrotron self-Compton (short-dashed) and external Compton (dot-dashed).

TeV, with high polarisation (at both optical and radio frequencies) and high brightness temperatures. These objects are sub-classified into Flat-Spectrum Radio Quasars (FSRQs) and BL Lacertae Objects (BLOs).

### 1.5.1 Flat-Spectrum Radio Quasars

FSRQs have strong, broad emission lines and have active accretion discs. They possess smaller black hole masses and are more luminous than BLOs with lower particle acceleration in the jets. The average viewing angle of FSRQs is 4° (Lister et al. 2009). All FSRQs tend to have flat radio spectra typically with $\alpha > -0.5$, for $S_\nu \propto \nu^\alpha$. Their continuum emission shows the presence of a "blue bump" in the SED and is characterised by rapid variability, high and variable polarisation, high brightness temperatures and relativistic shocks in radio jets. FSRQs can be

sub-divided as Optically Violently Variables, Highly Polarised Quasars and Core-Dominated Quasars. However, various observations have shown that these three different classes reflect the same properties and hence are always called by their parent population, the FSRQs (Fugmann 1988; Valtaoja et al. 1992b; Wills et al. 1992).

### 1.5.2 BL Lacertae Objects

BLOs lack strong emission lines in their optical spectra (typical equivalent width limits are set at less than 5 Å), which makes the determination of redshift very difficult. The jet energetics are stronger in BLOs with higher particle acceleration compared to the FSRQs while the accretion disc emission is very weak. The average viewing angle of the jet in the BLOs is 9° (Lister et al. 2009). Based on the discovery of these objects in the radio or X-ray band, they have been classified into radio- (RBL) or X-ray selected BLO (XBL). RBLs are more luminous in radio and optical wavebands, and have a higher degree of polarisation compared to the XBLs (Stocke et al. 1985). The presence of a third class that is intermediate between RBL and XBL has recently gained popularity. The peak frequency for RBLs and XBLs are in the radio/infrared and Ultraviolet/X-ray bands, respectively, while the intermediate BLOs peak in the optical wavebands. Thus, considering the physical difference between the different categories, the source class was revised into low- and high-frequency-peaked BLOs (Padovani & Giommi 1995).

The classification of BLOs discussed above can be revised to be based on the location of the synchrotron peak, $\nu_{\rm syn}^{\rm pk}$. The $\nu_{\rm syn}^{\rm pk}$ span a range from $\sim 10^{12}$–$10^{18}$ Hz. The three classes are: low synchrotron peaked (LSP) with $\nu_{\rm syn}^{\rm pk} \lesssim 10^{14}$ Hz, intermediate synchrotron peaked (ISP) with $10^{14} \lesssim \nu_{\rm syn}^{\rm pk} \lesssim 10^{15}$ Hz, and high synchrotron peaked (HSP) blazars with $\nu_{\rm syn}^{\rm pk} \gtrsim 10^{15}$ Hz. The sketch of the blazar SED with the three classes are shown in Figure 1.5.

The emission mechanism at X-rays in LSPs, ISPs and HSPs are dominated by inverse-Compton, synchrotron and inverse-Compton, and synchrotron processes, respectively. In LSPs, the X-ray spectrum is flat ($\alpha_X \lesssim 1$), while in HSPs it is steeper ($\alpha_X \approx 1.5$). On considering the two primary classes of blazars, the $\nu_{\rm syn}^{\rm pk}$ in FSRQs are always $\lesssim 10^{14}$ Hz and hence only belong to the class LSP. BLOs show great scatter in the distribution of the $\nu_{\rm syn}^{\rm pk}$ and can be classified into any of the three types (e.g. Nieppola et al. 2006; Giommi et al. 2012).

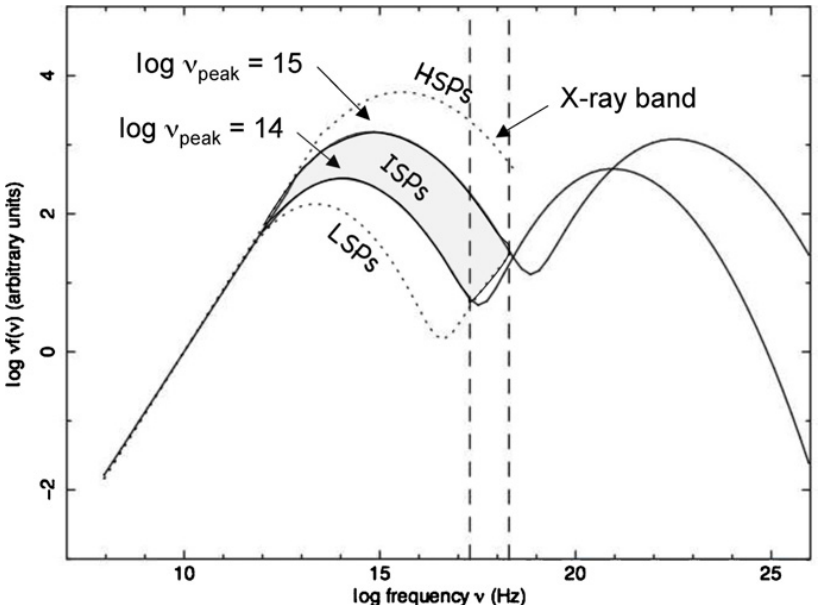


**Figure 1.5.** Different blazar types based on the peak of the synchrotron component in their SED. Low synchrotron peaked blazars, LSP, are denoted by the lower dotted line and high synchrotron peaked blazars, HSP, is dotted line by the upper dotted line. Intermediate synchrotron peaked sources, ISP, are confined within the gray area. Credit: Abdo et al. (2010b)

## 1.6 Emission Mechanisms

The emission from blazars has been observed from radio frequencies all the way to TeV $\gamma$-rays. Different regions in a blazar radiate at different frequencies (Figure 1.6). To understand the physical mechanism of a blazar emission across the electromagnetic spectrum, various models have been proposed. All of them assume the emission to be thermal or non-thermal in nature. The latter emission is produced by two processes – synchrotron and inverse-Compton.

### 1.6.1 Thermal radiation

Due to the turbulence and change in the gravitational potential energy of the infalling material, the accretion disc is heated to high temperatures ($\sim 10^5$ K) such that it can emit thermal radiation with energies all the way up to the X-ray part of the spectrum. Also referred to as the *bremsstrahlung* (braking radiation in German) or free-free emission, they are produced via the interaction of an electron with a free ion. This interaction results in a change in the momentum that accelerates the particles

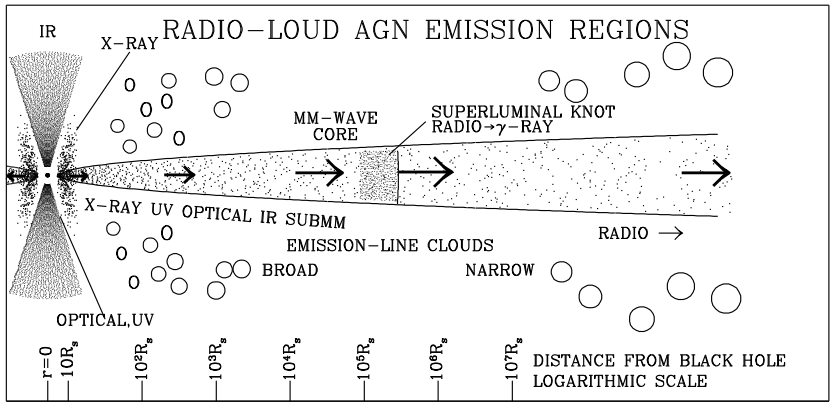


**Figure 1.6.** Emission regions of a radio-loud AGN from Marscher (2005).

to produce the observed radiation. Thermal emission can emerge from different regions of the central engine of AGN. Thermal continuum emission in the ultraviolet and optical bands is believed to originate within the accretion disc, while those in the infrared bands is believed to originate in the dusty, molecular torus, representing emission from the disc or BLR that has been reprocessed in this optically thick region into thermal radiation (see Antonucci 1993, for a review).

### 1.6.2 Synchrotron mechanism

The magnetic fields in AGN are likely formed due to ionised particles from the accretion disc in-falling towards the black hole. Due to the rotation of the disc, the magnetic field lines form a helical spiral. When charged particles spiral up the magnetic field lines, they emit synchrotron radiation. The emission is along the direction of the electron's motion. The emission due to beaming effects will be radiated along a narrow cone with an opening angle, $\phi \simeq \Gamma^{-1}$, and the observer detects the emission when the cone sweeps along the line of sight. The radiation will be more beamed with an increase in the Lorentz factor.

The peak synchrotron frequency, $\nu_{\rm syn}^{\rm pk}$, for an electron is given by

$$\nu_{\rm syn}^{\rm pk} \approx \frac{Be}{2\pi m_e c}\gamma^2, \tag{1.6}$$

where $B$ is the magnetic field, $e$ and $m_e$ are the charge and mass of an electron. For highly relativistic electrons, this reduces to

$$\nu_{\rm syn}^{\rm pk} \equiv \gamma^2 \nu_g. \tag{1.7}$$

where $\gamma$ is the electron Lorentz Factor and $\nu_g$ is the gyrofrequency.

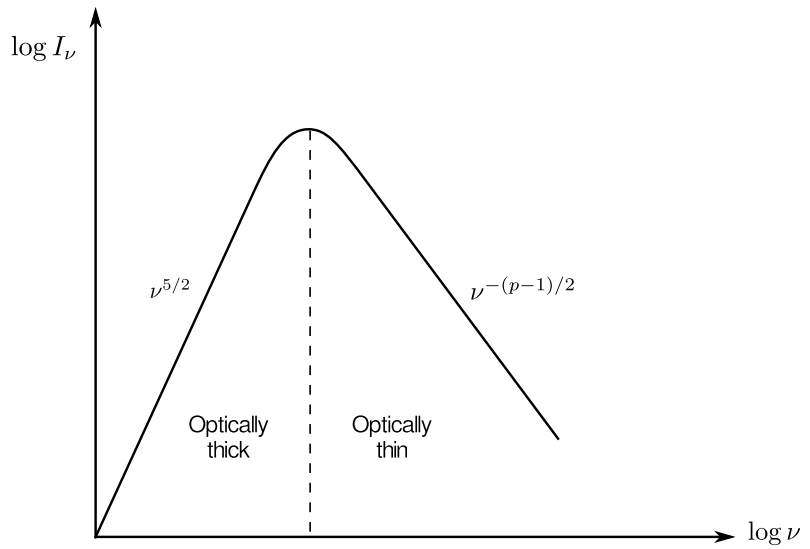


**Figure 1.7.** The spectrum produced by synchrotron emission for electrons with power-law distribution. The optically thick part is given by $\nu^{5/2}$, and the optically thin part is described by $\nu^{-(p-1)/2}$. Credit: Rybicki & Lightman (1979).

*Synchrotron self-absorption:* A synchrotron source with brightness temperature $T_{\rm b} > m_e c^2/k \approx 10^{10}$ K will become self-absorbed at low-frequencies and below the turnover frequency, $\nu_m$. This process occurs when relativistic electron absorbs and emits the photons they are producing. For non-thermal electron distribution, the synchrotron self-absorption increases with decreasing frequency. Thus, the synchrotron emission becomes optically thick below turnover frequency. For electrons with power-law distribution, the optically thick spectrum becomes $S_\nu \propto \nu^{5/2}$. At high frequencies, the radiative losses dominate the steepening of the electron energy distribution. The resulting spectrum is shown in Figure 1.7. For more discussion on the topic and derivation of the equations, see Rybicki & Lightman (1979).

### 1.6.3 Inverse-Compton Scattering

In Compton scattering, an electron scatters off a photon and in turn gains energy. Its opposite, i.e. when a low-frequency photon gains energy, is called the inverse-Compton scattering (ICS). The location of the seed photons in ICS process producing $\gamma$-ray emission is still under scrutiny. This is due to the concerns over the source of seed photons when the emission region is closer to the supermassive black hole and the source of electrons

if the emission region is in the parsec-scale radio-jet. Through numerous modelling efforts, the source of photons near the supermassive black hole can be constrained to: optical/UV photons from an accretion disc (e.g. Dermer et al. 1992), optical photons from the BLR, and infrared dust photons (Sikora et al. 1994; Błażejowski et al. 2000). The emission mechanism in these cases is referred to as external inverse-Compton (EIC). In the other scenario, the synchrotron photons can be produced in the jet through synchrotron processes, thus, serving as seed photons for ICS. This process is called synchrotron self-Compton (SSC; e.g. Maraschi et al. 1992; Bloom & Marscher 1996).

*Synchrotron self-Compton:* The spectrum of an SSC process is smooth and broad, similar to those of the synchrotron process that provides the seed photons which are up-scattered to high-energies. Hence, the variability of a synchrotron and SSC-dominated process should be the same, and so is the peak luminosity, which can also be understood from the SED in Figure 1.4. The luminosity of an SSC process assuming an isotropic distribution of photons is given by

$$L_{\rm SSC} = \frac{4}{3}\sigma_{\rm T} c U_{\rm ph} \Gamma^2 \beta^2 \tag{1.8}$$

where $\sigma_{\rm T}$ is the Thomson cross section and $U_{\rm ph}$ is the energy density of the photon field. The synchrotron luminosity is given by

$$L_{\rm synch} = \frac{4}{3}\sigma_{\rm T} c U_B \Gamma^2 \beta^2 \tag{1.9}$$

where $U_B$ is the energy density of the magnetic field. From equations (1.8 and 1.9, it is clear that in the Thomson limit the synchrotron and SSC radiations are related as

$$\frac{L_{\rm synch}}{L_{\rm SSC}} = \frac{U_B}{U_{\rm ph}}, \tag{1.10}$$

i.e. the relative emission of the synchrotron and SSC mechanisms are dependent on the magnetic field energy density and the photon field energy density in the source. The luminosity of the SSC component is stronger for compact emission regions, and it decreases with any increase in the size of the emission region. The discussed scenario for the SSC processes are under a one-zone model where a single plasma blob acts as an emission region of size, $R = ct_{\rm var}\delta/(1+z)$ where $t_{\rm var}$ is the variability time-scale. In certain cases, the up-scattered photons may act as a seed photon field thus triggering multiple SSC scattering (see Björnsson 2010, for more discussion).

*External inverse-Compton:* In this case, the seed photon field for Compton scattering is located closer to the central engine. The ICS of electrons

on these photons pushes the high-energy hump of the SED to higher flux values. This dominance of the EIC component over the synchrotron can be understood from the SED of 3C 279 shown in Figure 1.4. The relation between the EIC and synchrotron luminosities can be expressed as

$$\frac{L_{\rm synch}}{L_{\rm EIC}} = \frac{U_B}{U'_{\rm ph}}, \tag{1.11}$$

where $U'_{\rm ph}$ invokes the relative speed between the relativistic electrons and photon field. In general, EIC seems to be prerogative of the high-energy emission in FSRQs, just like the SSC is the favoured model for BLOs (e.g. Abdo et al. 2010b).

Both SSC and EIC processes are classified under the leptonic models where the Compton scattering of low-energy photons from the ultrarelativistic electrons dominates the high-energy emission. In the hadronic model, the photo-pair and photo-pion production due to the presence of ultrarelativistic protons in the jet will initiate cascades that dominates the high-energy emission (see Böttcher et al. 2013, for a review). Throughout this thesis only the correlated variability in blazars is explored, which are predicted under the leptonic models. Therefore, the hadronic model will not be accounted for any of the analyses.

## 1.7 Multifrequency Connection

The investigation of blazar variability from radio to $\gamma$-ray frequencies provides information regarding the connection between these wavebands and can also explain the emission mechanism in the $\gamma$ rays.

### 1.7.1 *CGRO*/EGRET era

The *Compton Gamma-Ray Observatory* (CGRO) was the first major space observatory dedicated to observations in the $\gamma$ rays. It operated between 1991 and 2000. The Energetic Gamma-Ray Experiment Telescope (EGRET) was one of the instruments onboard the CGRO that observed in the energy range 20 MeV to 30 GeV. The all-sky survey performed by EGRET was completed in 1999 and released the third EGRET catalogue (Hartman et al. 1999). The instrument detected 271 sources of which 66 were blazars.

Many differing statistical analyses of these EGRET-detected blazars have been conducted with some of them concentrating on the direct relationship between the radio and $\gamma$-ray luminosities (e.g. Muecke et al. 1997;

Bloom 2008). Through a comprehensive statistical analysis, Bloom (2008) showed that the radio and $\gamma$-ray luminosities are related as: $L_\gamma \propto L_r^{0.77\pm0.03}$. Using Monte Carlo simulations, the author was able to replicate the observed luminosity relationship, under the assumption of an SSC model.

Using single-dish radio observations, Valtaoja & Teräsranta (1995) suggested that the radio and the $\gamma$-ray flares must be produced in the same shocked regions in the jet. Their inference was based on the EGRET detection during the rising phase or peak of the radio flare. On the other hand, Lähteenmäki & Valtaoja (2003) concluded that the $\gamma$ rays were produced downstream from the radio core. These results also agree with those obtained from VLBI observations of the shocked regions in the jet (Jorstad et al. 2001b). Thus, all these findings are in favour of the SSC mechanism for the $\gamma$-ray emission.

### 1.7.2 *Fermi* /LAT era

Launched in 2008, the *Fermi Gamma-Ray Space Telescope* is the successor to the CGRO. The Large Area Telescope (LAT) onboard the *Fermi* is the primary instrument capable of observing in the energy range, 20 MeV to 300 GeV (Atwood et al. 2009, hereafter *Fermi* /LAT). The field of view of *Fermi* /LAT is about 20 per cent of the sky. Owing to the better sensitivity, larger field of view and, more importantly, the faster scanning strategy (scans continuously the whole sky every three hours) of *Fermi* /LAT over CGRO/EGRET, $> 500$ blazars were detected within the first two years of operation (hereafter 2FGL; Nolan et al. 2012).

Even with one year of the *Fermi* /LAT observations, several studies were made regarding the radio and $\gamma$-ray connection in blazars. Kovalev et al. (2009) using three months of data was able to establish the correlation between *Fermi* /LAT photon flux and quasi-simultaneous 15 GHz flux density observations. They conclude that the $\gamma$-ray emission is strongly correlated with the parsec-scale radio emission in bright $\gamma$-ray objects. This result also agrees with those obtained from VLBI observations, which shows the presence of superluminal speeds, large opening angles and high Doppler factors in *Fermi* /LAT detected blazars.

Using the first *Fermi Gamma-Ray Catalogue* (Abdo et al. 2010a), Nieppola et al. (2011) showed the existence of flux and luminosity correlation using 37 GHz radio observations. Meanwhile, by comparing the onset of the millimetre flare to the $\gamma$-ray peak for 60 bright northern blazars, León-Tavares et al. (2011) constrained the $\gamma$-ray emission region to the parsec-

scale radio jet. Due to the uniform and densely sampled *Fermi*/LAT light curves, time variability studies have been performed in connection with the radio, millimetre and optical light curves (Cohen et al. 2014b; Fuhrmann et al. 2014; Max-Moerbeck et al. 2014a). Likewise, several simultaneous observing campaigns have been organised to study the spectral variability of blazars (Abdo et al. 2010b).

## 1.8 Importance of Blazar Research

The precipitous amount of radiation from the black hole-powered objects and the high temperatures prevailing around them cannot be found elsewhere in the Universe. Hence, the study of objects, such as blazars offers an opportunity for understanding the energy production mechanism that is associated with the black hole, which today still remains an enigma.

The emission from relativistic jets in blazars is characterised by extreme variability across the electromagnetic spectrum. Associated with this property are the physical phenomenon, such as the collimation of the jet, the propagation of shocks, acceleration of relativistic particles and the ICS of photons to high-energies. Over decades of observational support and numerical modelling, the astronomical community has come to a consensus regarding the emission mechanisms in the radio to X-ray bands, the relativistic property of the jets and the presence of magnetised plasmas in jets. This knowledge still precludes us from understanding the formation and collimation of the jet, accretion processes in AGN, activity cycle of the black hole and the high-energy emission mechanisms, among others.

In this thesis, I address the high-energy emission mechanism in blazars using multifrequency observations and time variability analysis. The well-sampled data of most sources allowed in constraining the physical and variability properties, along with a hint on the location of the photon field for the high-energy emission.

# 2. Multifrequency Observations and Data Reduction

## 2.1 Gamma-ray observations

The $\gamma$-ray data used throughout this thesis have been obtained from the *Fermi* /LAT instrument. The LAT with an energy range of 20 MeV to 300 GeV has an energy resolution <15 per cent at energies >100 MeV. The effective area of the LAT is >8000 cm$^2$ for photons incident at an angle, $\theta = 0$. The point source sensitivity is $< 6 \times 10^{-9}$ photons cm$^{-2}$ s$^{-1}$ for energies >100 MeV. The LAT is a pair conversion instrument that creates an electron-positron pair from the incident photon. The instrument allows the photon to go through the conversion foils followed by the particle tracking detectors where it interacts with tungsten to form an electron-positron pair. Finally, their energies are determined by a calorimeter. The $\gamma$-ray photons incident on the detector can be contaminated by the cosmic ray particles that dominate over the photons by a magnitude of the order greater than three. To overcome this issue, the LAT instrument consists of an anti-coincidence detector that can identify the cosmic rays, which are excluded from the analysis.

The $\gamma$-ray fluxes can then be obtained from the FITS files provided by the *Fermi* Science Support Center[1]. In Publications I–III, I obtained the $\gamma$-ray fluxes over the energy range of 0.1–200 GeV using the SCIENCE TOOLS[2]. Following the data selection recommendation[3], only photons with event class of 2 (corresponds to higher probability of being photons) were chosen while excluding those with zenith angle $> 100^\circ$ to avoid contamination from photons coming from the Earth's limb. The instrument

[1] http://fermi.gsfc.nasa.gov/ssc/
[2] http://fermi.gsfc.nasa.gov/ssc/data/analysis/documentation/Cicerone
[3] http://fermi.gsfc.nasa.gov/ssc/data/analysis/scitools/data_preparation.html

response functions P7REP_SOURCE_V15 were used throughout (Ackermann et al. 2012).

An unbinned likelihood methodology was implemented using *gtlike* (Cash 1979; Mattox et al. 1996). This task models all sources including the target source within the region-of-interest ($15^{\circ}$) obtained from the 2FGL. The model parameters of sources with significance $< 2\sigma$ were fixed to the 2FGL value while those of other sources were allowed to vary. The Galactic diffuse emission, and the isotropic background (sum of extragalactic diffuse and residual instrumental backgrounds) were also modelled at this stage, using the template provided with the SCIENCE TOOLS. The final fluxes were then obtained from this analysis along with the source detection criterion given by the maximum-likelihood test statistic (TS; Mattox et al. 1996). TS is given as $-2\ln(L_{max,0}/L_{max,1})$, where $L_{max,1}$ and $L_{max,0}$ corresponds to the maximum likelihood value for a model with and without an additional source. For bins with TS less than nine in Publication I, $2\sigma$ upper limits were estimated using a profile likelihood method (Rolke et al. 2005).

### 2.2 X-ray observations

The X-ray data was obtained from the *Swift* X-ray Telescope (XRT). The instrument can observe over the energy range of 0.2–10 keV, and has a sensitivity limit of $2 \times 10^{-14}$ to $9 \times 10^{-10}$ erg cm$^{-2}$ s$^{-1}$. At 1.5 keV, the telescope has an effective area of 110 cm$^2$ and a resolution of 18 arcsec. The X-ray data used for this thesis were obtained from a monitoring programme of *Fermi* blazars in the energy range, 0.3–10 keV. The X-ray data reduction method is discussed in Williamson et al. (2014).

### 2.3 Optical observations

The optical data used in Publication I were gathered from various observatories at wavebands *B-, V-, R-* and *I*-band. These data were part of a monitoring programme of *Fermi* blazars. The optical facilities include the Catalina Real-time Transient Survey (Drake et al. 2009)[4], Lowell Observatory (1.83-m Perkins Telescope equipped with the PRISM camera), Calar Alto (2.2-m Telescope, observations under the MAPCAT[5] pro-

[4] http://crts.caltech.edu/

[5] http://www.iaa.es/∼iagudo/research/MAPCAT

gramme), Liverpool 2-m Telescope, Crimean Astrophysical Observatory (0.7-m Telescope), and St. Petersburg State University (0.4-m Telescope). The optical data analysis procedures except for the Catalina data were performed as discussed in Jorstad et al. (2010).

For Publication III, the $R$-band data were obtained from the Tuorla blazar monitoring programme[6], Steward Observatory of the University of Arizona[7] (observations under the ground-based observational support of the *Fermi Gamma-ray Space Telescope*) and from the Yale University SMARTS[8] programme.

### 2.4 Radio observations

For studying the radio and $\gamma$-ray connection of 1156+295 in Publication I, the 230 GHz (1.3 mm) light curve from the Submillimeter Array (SMA) was used. The SMA is an 8-element radio interferometer located in Hawaii, with each antenna sizing up to 6 m. The longest baseline extends as far as 509 m. The frequency range of the array is from 180 to 700 GHz that has a sub-arcsecond resolution. Observations at the SMA are calibrated against known standards, typically solar system objects (Titan, Uranus, Neptune or Callisto). Data from this programme are regularly updated and are available at the SMA website[9].

In Publication III, 95 GHz observations from the Combined Array for Research in Millimeter-wave Astronomy (CARMA) interferometer was used. CARMA consists of eight 3.5 m telescopes capable of observing at a central frequency of 95 GHz with a bandwidth of 7.5 GHz. The data were reduced using the MIRIAD software (Sault et al. 1995), including standard bandpass calibration on a bright quasar. The amplitude and phase gain calibration was done by self-calibrating on the target source. The absolute flux calibration was determined from a temporally nearby observation (within a day) of the planets Mars, Neptune or Uranus, whenever possible. Otherwise, the sources 3C 273, 3C 345, and 3C 84 were used as secondary calibrators. The CARMA observations were taken as part of the Monitoring of $\gamma$-ray Active galactic nuclei with the Radio, Millimetre and Optical Telescopes[10] programme.

[6] http://users.utu.fi/kani/1m/index.html
[7] http://james.as.arizona.edu/~psmith/Fermi/
[8] www.astro.yale.edu/smarts/glast/home.php
[9] http://sma1.sma.hawaii.edu/callist/callist.html
[10] http://www.astro.caltech.edu/marmot/

The 37 GHz observations were obtained with the 13.7 m diameter Metsähovi radio telescope, which is a radome-enclosed paraboloid antenna situated in Finland. The measurements were made with a 1 GHz-band dual beam receiver centred at 36.8 GHz. The observations are ON–ON observations, alternating the source and the sky in each feed horn. A typical integration time to obtain one flux density data point is between 1200 and 1400 s. The detection limit of the telescope at 37 GHz is on the order of 0.2 Jy under optimal conditions. Data points with a signal-to-noise ratio $< 4$ are handled as non-detections and discarded from the analysis. The flux density scale is set by observations of the HII region DR21, with a known flux density of 17.9 Jy at 37 GHz (Teräsranta et al. 1998). The sources NGC 7027, 3C 274 and 3C 84, are used as secondary calibrators. A detailed description of the data reduction and analysis is given in Teräsranta et al. (1998).

### 2.4.1 VLBA observations

To investigate the kinematics of the inner regions of the jet in the blazar 1156+295, 47 VLBA observations at 43 GHz from the Boston University blazar monitoring programme[11] were used. The data reduction and calibration were performed as discussed in Jorstad et al. (2005).

The calibrated data was obtained from their archive and the complex visibilities were then modelled with multiple components using the task *modelfit* in the DIFMAP program (Shepherd 1997), with each model represented by a simple two-dimensional Gaussian brightness distribution. This method can identify components of the source structure that are closer than the resolution of the synthesized beam but are resolved by the longest baselines. The model consisted of circular Gaussian components to parametrize the data to reduce the number of free parameters. The fit was considered to be good if the residual map rms-noise was low, and the reduced $\chi^2$ statistic was $\sim 1$. A fit to an additional component was deemed necessary only if it significantly improved the quality of the fit. No starting model was used during the modelfit procedure. The uncertainties of the parameters of individual components were estimated with the DIFWRAP package (Lovell 2000), following the approach discussed in Rastorgueva et al. (2011).

[11] http://www.bu.edu/blazars/VLBAproject.html

## 2.5 *Planck* observations

The *Planck* satellite, launched in 2009, mapped the cosmic microwave background radiation with high precision. Apart from that, the all-sky scanning strategy employed by *Planck* provides a uniform sampling and allows one to study the distant galaxies in microwave to submillimetre wavelengths. The primary mirror of *Planck* is 1.9 $\times$ 1.5 m in diameter with an effective aperture size of 1.5 m. The telescope possesses two instruments – Low Frequency Instrument (LFI) and High Frequency Instrument (HFI). The LFI can observe in the frequency range of 27 to 77 GHz with the best resolution of 14 arcmin at 70 GHz. The HFI observes in the frequency range of 84 GHz to 1 THz. The best resolution that can be achieved with HFI is 5 arcmin at 857 GHz. During the *Planck* observing

**Table 2.1.** Multifrequency data used in Publication IV

| Observatory | Frequencies (GHz) |
|---|---|
| *Planck* LFI | 30, 44, 70 |
| *Planck* HFI | 100, 143, 217, 353, 545, 857 |
| Metsähovi, Finland | 37 |
| OVRO, USA | 15 |
| RATAN-600, Russia | 1.1, 2.3, 4.8, 7.7, 11.2, 21.7 |
| UMRAO, USA | 4.8, 8.0, 14.5 |

period a multifrequency campaign to study the spectral evolution of the bright AGN was initiated. All the data that was used as part of this work (Publication IV) is shown in Table 2.1. In total there were four surveys from August 2009 to August 2011.

# 3. Statistical tests for variability

## 3.1 Power Spectral Density

The PSD analysis is one of the methods to characterise the time variability. PSD is defined as a function of frequency measuring their respective contributions to the overall variability of a varying signal.

The PSD of an evenly sampled light curve is the amplitude squared of the light curve's Fourier transform. Since such continuity in the time series is almost never observed, the PSD can be approximated by its mathematical analogy, the periodogram. For a light curve of length $N$, the periodogram is given by the modulus squared of the discrete Fourier transform of the data (DFT; Press et al. 1992) as defined by

$$DFT(j) = \sum_{k=1}^{N} x(t_k)\, e^{2\pi i(k-1)j/N}. \tag{3.1}$$

The periodogram, $P(f_j)$, at a Fourier frequency of $f_j$, is given by

$$\begin{aligned} &P(f_j) = \frac{2}{N^2}\left\{\mathrm{Re}[\mathrm{DFT}(j)]^2 + \mathrm{Im}[\mathrm{DFT}(j)]^2\right\} \\ &\text{even } N : j = 0, 1, \ldots, N/2 \\ &\text{odd } N : j = 0, 1, \ldots, (N-1)/2 \end{aligned} \tag{3.2}$$

where $f_j$ = $j/(N\Delta T_{\mathrm{bin}})$ and $\Delta T_{\mathrm{bin}}$ is the binning interval of the light curve. For even $N$, $f_{N/2}$ = 1/(2$\Delta T_{\mathrm{bin}}$) is the Nyquist frequency, $f_{\mathrm{Nyq}}$. The zero Fourier frequency component, $f_0$, corresponds to the sum of the light curve.

Many conventions exist for the overall normalisation of the periodogram (see Vaughan et al. 2003, for more information). The fractional rms normalisation, $N\Delta T_{\mathrm{bin}}/\mu^2$, is one widely used in the periodogram. The contribution to the fractional rms-squared variance (i.e. $\sigma^2/\mu^2$) due to variations from the corresponding time-scales (Miyamoto et al. 1991; van der Klis

1997) can be obtained with this normalisation. This can be inferred by taking the square root of the integral of the underlying PSD between two frequencies $f_1$ and $f_2$. Thus, the total rms-squared variability is obtained by integrating between $f_1$ and $f_{\rm Nyq}$ (even) or $f_{(n-1)/2}$ (odd). Equation (3.2) therefore reduces to equation (3.3).

$$P(f_j) = \frac{2\Delta T_{\rm bin}}{\mu^2 N} \left\{ {\rm Re}[{\rm DFT}(j)]^2 + {\rm Im}[{\rm DFT}(j)]^2 \right\}. \tag{3.3}$$

The underlying PSD for AGN light curves are, in general, assumed to be distributed as a power-law of the form: $P(f) \propto f^{-\alpha}$. The simplest approach to estimating the PSD slope, $\alpha$, is by fitting a straight line to the logarithmically transformed and binned periodogram as discussed in Papadakis & Lawrence (1993). This approach reduces the scatter in the periodogram and thus reduces the effect of outliers on the fitting. However, taking logarithm also introduces a bias to the power of the periodogram that can be removed by adding a constant 0.25068 (Vaughan 2005) to obtain the final binned logarithmic periodogram. The binned logarithmic periodogram is normally distributed within each geometric mean frequency bin.

As long as the light curves are evenly sampled, the underlying PSD of the light curve can be estimated by fitting a power-law to the periodogram, or by fitting a straight line to the periodogram in logarithmic scale. However, owing to the uneven sampling in most cases, an additional bias contributes to the periodogram. Due to the finite length of the observed light curve, power from longer than observed time-scales leaks into the shorter time-scales and distorts the observed PSD. This process is called *red-noise leak*. On the other hand, uneven sampling of the light curve causes variations on time-scales down to the resolution of the observed light curve by *aliasing*. The power above $f_{\rm Nyq}$ which is aliased to frequencies below $f_{\rm Nyq}$ makes the observed periodogram distorted.

Due to these added uncertainties in an unevenly sampled light curve, a variant of the Power Spectral Response method proposed by Uttley et al. (2002) for estimating the PSD is discussed here. This method involves the simulation of light curves for a set of model parameters, followed by the estimation of the periodogram for every simulated light curve and then averaging them and, finally, determining the best-fitting PSD from a goodness of fit. The method is discussed in detail in the following subsections.

### 3.1.1 Estimation of the Periodogram for unevenly sampled light curve

To estimate the periodogram, every light curve ($\{t_k, x(t_k)\}$ for $k$ = 1,2,. . . ,$N$) is initially binned in time intervals $\Delta T_{\rm bin}$, by taking the weighted mean of all points within each bin. Any missing data points in the binned light curve can be linearly interpolated. The computation of the periodogram is a product of a window function, $w$(t), and the observed light curve. The window function is equal to one when there is an observation and zero otherwise. Thus, for an evenly sampled light curve, this poses no threat to the periodogram unlike when the light curve is unevenly sampled. To tackle the impact of *red-noise leak* on the binned light curve, Max-Moerbeck et al. (2014b) recently proposed an approach by convolving the binned light curve with a Hanning window function of the form

$$w_{\rm Hanning}(t) = \begin{cases} 0.5(1 - \cos(2\pi\frac{t}{T})), & 0 \leq t \leq T \\ 0, & \text{otherwise.} \end{cases} \tag{3.4}$$

At this stage, the light curve will be evenly sampled. The periodogram can then be computed using the equation (3.3). The final observed periodogram, $P_{\rm obs}(f)$, can be obtained by logarithmically transforming and binning the periodogram while also accounting for the bias.

### 3.1.2 Simulating Light Curves

To simulate an AGN light curve, a power spectral model such as a power-law, is chosen to test against the data. The normalisation of the model power spectrum is a multiplicative factor that is carried through any convolution with the window function (i.e. only the power spectral shape is distorted by sampling).

The effect of *red-noise leak* can be taken into account by simulating light curves at least 100 times longer than the observed light curve. The impact of *aliasing* can be accounted for by simulating light curve with time resolution higher than the observed. Hence, throughout this thesis, the sampling time, $\Delta T_{\rm samp}$, was considered to be 10 per cent of the original estimate. The light curve simulated with this sampling time can be re-sampled by considering only those measurements at times identical to the observed ones. Thus, the factor 10 per cent used here was sufficient to introduce uneven sampling by obviating the need to extrapolate the data, which would have been necessary for any factor higher than 10 per cent.

Although the resolution can be improved by lowering the factor it doesn't affect the resampled light curve other than the sunk costs of computation by being time-consuming and memory-intensive.

Taking into account the ramifications of the PSD estimation discussed above, $N$ light curves (with $N$ at least being 100), assuming to be distributed as a power-law can, be simulated using the method proposed by Emmanoulopoulos et al. (2013, hereafter EMP13). The widely used algorithm of Timmer & Koenig (1995, hereafter TK95) for simulating light curves is appropriate for the production of Gaussian light curves. Since the distributions of most of the light curves are far from being Gaussian, especially in the X-rays and $\gamma$ rays, light curves simulated using the method by TK95 may not be appropriate for the establishment of confidence intervals for the PSD and cross-correlation studies. The method by EMP13 involves the combination of the routine by TK95 and the iterative amplitude adjusted Fourier transform algorithm by Schreiber & Schmitz (1996), producing light curves possessing exactly the PSD and the probability density function (PDF) as the observed light curve. The simulation of light curve using the EMP13 method is as follows:

(i) As the first step, a Gaussian distributed light curve, $x_{\rm norm}(t)$, of length $N$ with an underlying PSD of slope $\alpha$ is produced using the TK95 procedure. The amplitude ($\mathscr{A}_{\rm norm}(j)$) and phase ($\phi_{\rm norm}(j)$) of $x_{\rm norm}(t)$ is obtained through the DFT, $DFT_{\rm norm}(j)$.

(ii) To account for the distribution of the original light curve, $N$ pseudo-random numbers, $x_{\rm sim,1}(t)$, is produced from the PDF $[0 \leq x_{\rm obs}(t) < \infty]$. Similar to the step above, the corresponding amplitudes, $\mathscr{A}_{\rm sim,1}(j)$, and phases, $\phi_{\rm sim,1}(j)$, at each Fourier frequency $f_j$, through the DFT of $x_{\rm sim,1}(t)$ can be obtained.

(iii) **Spectral adjustment**: Having generated two surrogate data, one can perform phase randomisation to obtain an adjusted DFT of $x_{\rm sim,1}(t)$, $DFT_{\rm sim.adjust,1}(j)$, by replacing the amplitudes, $\mathscr{A}_{\rm sim,1}(j)$ with $\mathscr{A}_{\rm norm}(j)$ at each frequency $f_j$, while keeping the phases $\phi_{\rm sim,1}(j)$ unaltered. In order to obtain a surrogate data with underlying PSD to those used in step (i), an inverse DFT should be performed on $DFT_{\rm sim.adjust,1}(j)$, thus yielding $x_{\rm sim,adjust,1}(t)$. This step is similar to using a filter in the frequency domain. At this point, $x_{\rm sim,adjust,1}(t)$ is scaled and standardised based on the statistical moments such as the mean and variance of the observed data.

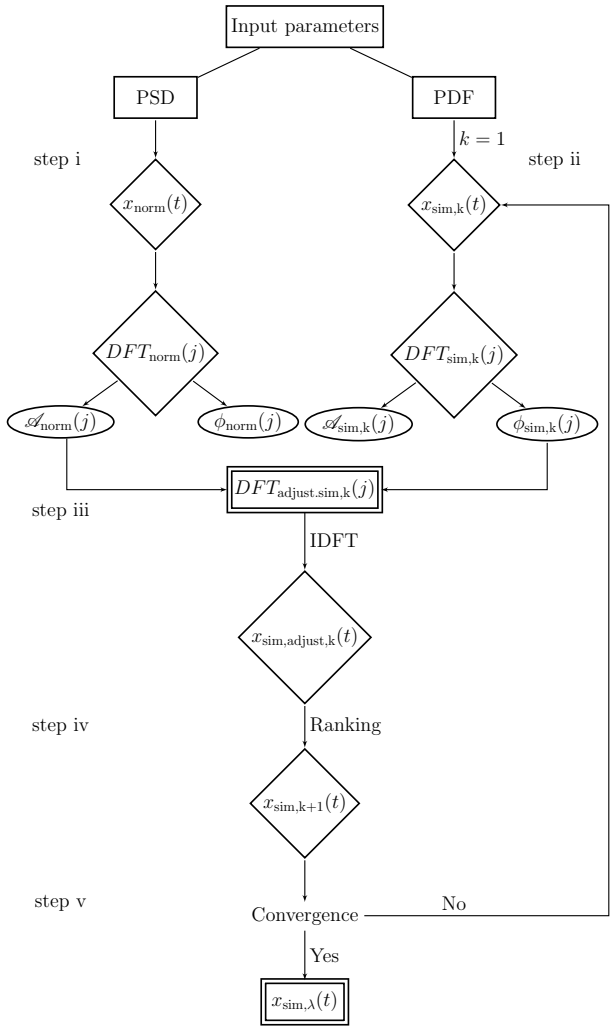


**Figure 3.1.** Flowchart showing the various steps for the simulation of a light curve from Emmanoulopoulos et al. (2013).

(iv) **Amplitude adjustment**: Since the surrogate data generated in the step above has its PDF altered from those that was generated in step (ii), $x_{\rm sim,1}(t)$ should be sorted based on the ranking of $x_{\rm sim.adjust,1}(t)$. This replaces the highest value of $x_{\rm sim.adjust,1}(t)$ by the highest value of $x_{\rm sim,1}(t)$ and so on, while also ensuring the desired PDF of the surrogate data. The caveat here is that the PSD is modified from those of step (iii).

(v) To ensure the amplitude adjusted surrogate data to have the desired PSD and PDF, they are scaled and standardised. The above steps are then iterated from step (ii) with a modification of using the amplitude adjusted data as $x_{\rm sim,1}(t)$. The final simulated data is obtained only when there is a convergence such that $x_{\rm sim,k+1}(t) \equiv x_{\rm sim,k}(t)$.

The flowchart of the EMP13 method is shown in Figure 3.1. For more information on the method see Emmanoulopoulos et al. (2013).

**Choice of Cumulative Distribution over Probability Density Function:** In the EMP13 algorithm, the random numbers are generated from the best-fitting PDF of the data, which is used during the amplitude adjustment stage. However, estimating the PDF of the data is not quite straightforward owing to the unknown number of modes present in the data. If one uses a histogram, one needs to choose the bin width and the starting point for the first bin. If one uses the kernel density estimation, one needs to select the kernel shape and bandwidth. Hence, to circumvent all the problems of obtaining a PDF, the cumulative distribution function (CDF) can be considered. The CDF has a simple non-parametric estimator that needs no choices to be made – the empirical distribution function. Therefore, random numbers can be generated using the CDF of the observed data. It is always better to confirm if the distribution of the generated random numbers agrees with those of the observed data by using, for example, a two-sample Kolmogorov-Smirnov test.

Finally, the simulated data can be normalised to the mean and variance of the observed light curve.

### 3.1.3 Goodness of fit

The simulated data is then resampled to the sampling pattern of the observed light curve. The Gaussian noise with zero mean and variance matching those of the observations, for radio to optical light curves, are

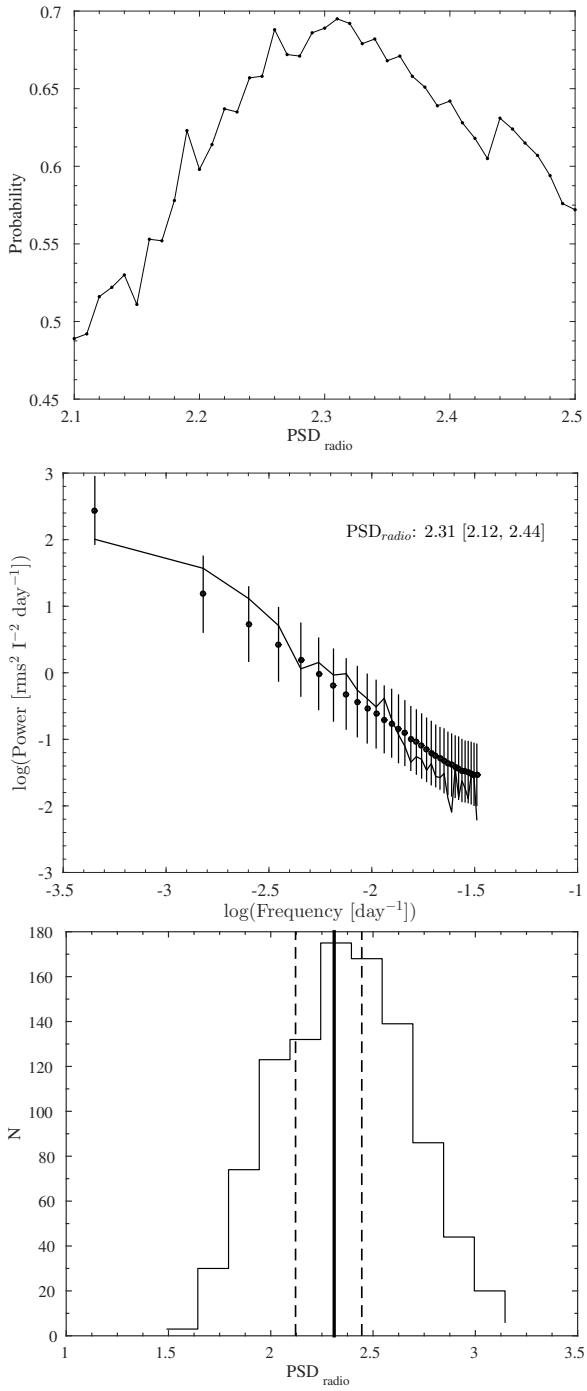


**Figure 3.2.** Three staged PSD analysis. *Top-panel:* Probability versus PSD. *Mid-panel:* PSD of observed light curve in solid line and those corresponding to the best-fitting PSD slope in circles with error bars. *Bottom-panel:* Distribution of PSD slope obtained from simulated light curves with best-fitting PSD slope; target PSD slope in solid line and $1\sigma$ confidence intervals in dashed lines.

added to the resampled light curves. For any photon counting experiments such as at X-rays and $\gamma$ rays, Poisson noise based on the bin width is added. The relation to the Poisson noise is according to the following equation

$$\mathrm{LC}_{\mathrm{sim}}(t_i) \sim \frac{\mathrm{Pois}[\mu = \mathrm{LC}_{\mathrm{sim}}(t_i)\Delta t]}{\Delta t} \text{ for } i = 1, \ldots, N \tag{3.5}$$

where $\mathrm{Pois}[\mu]$ corresponds to Poisson random number with a mean value of $\mathrm{LC}_{\mathrm{sim}}(t_i)\Delta t$. The tacit assumption of Gaussian distributed light curves after the resampling stage is common in many fields of astronomy. For such assumptions to be valid, one requires a significant number of points in a bin. However, it should be remembered that there is no straightforward conversion of a discrete distribution (e.g. Poisson) to the continuous one (e.g. normal). Hence, adding Poisson noise to data at X-rays and $\gamma$ rays are more appropriate. The resampled light curve is then subjected to the same procedure as employed to the observed light curve – binning with empty bins interpolated. The periodogram of the resulting light curve is then obtained using equation (3.3), and are subjected to the log-transformation and binning with bias correction. Thus for every simulated light curve a periodogram can be obtained. The binned logarithm periodograms are then averaged to obtain the model averaged periodogram, $\overline{P_{\mathrm{sim}}}(f)$, and the spread about the mean is also calculated and taken as the error in the power at each frequency, $\Delta\overline{P_{\mathrm{sim}}}(f)$.

After obtaining the model periodogram, a $\chi^2_{\mathrm{dist}}$ statistic as defined by Uttley et al. (2002) can be calculated from the model and observed periodogram, $P_{\mathrm{obs}}(f)$ with the following equation

$$\chi^2_{\mathrm{dist}} = \sum_{f=f_{\mathrm{min}}}^{f_{\mathrm{max}}} \frac{[\overline{P_{\mathrm{sim}}}(f) - P_{\mathrm{obs}}(f)]^2}{\Delta\overline{P_{\mathrm{sim}}}(f)^2}. \tag{3.6}$$

This step is followed by estimating the $\chi^2_{\mathrm{dist}}$ between the model and every simulated periodogram by replacing the $P_{\mathrm{obs}}(f)$ with $P_{\mathrm{sim},i}(f)$ (where $i$ = 1,2,. . . ,1000) in equation (3.6). The goodness of fit is given by the percentile of $\chi^2_{\mathrm{dist}}$ distribution from simulation that exceeds the observed $\chi^2_{\mathrm{dist}}$ estimate.

The entire process from simulating light curves to estimating the goodness of fit should be tested for a range of PSD values. The best-fitting PSD value corresponds to the one with the highest goodness of fit. To estimate the confidence intervals for this PSD value, one can simulate $N$ light curves using the EMP13 approach as discussed above, obtain their binned logarithm periodogram and estimate the PSD slope for each periodogram

by linear least squares method. The confidence interval can be obtained directly from the distribution of PSD slope. The results obtained from the whole chain is shown in the Figure 3.2.

## 3.2 Cross-correlation

To understand the variability and to probe the continuum emission mechanism of AGN, the cross-correlation function is employed. For evenly sampled light curves, the classical correlation function by Oppenheim & Schafer (1975) can be used. However, owing to various technical issues and seasonal gaps most of the light curves are unevenly sampled. To handle this problem, three variants of the classical function exist in literature – the Interpolated cross-correlation function (Gaskell & Peterson 1987), the discrete correlation function (DCF; Edelson & Krolik 1988) and the $z$-transformed discrete correlation function (Alexander 2013). Due to the unevenly sampled light curves used throughout this thesis, only DCF is considered. The DCF is estimated from the relation

$$\mathrm{DCF}_{ij} = \frac{(a_i - \bar{a})(b_j - \bar{b})}{\sigma_a \sigma_b} \ . \tag{3.7}$$

where $a_i, b_j$ are the observed fluxes at times $t_i$ and $t_j$ and $\bar{a}, \bar{b}, \sigma_a$ and $\sigma_b$ are the means and standard deviations of the entire light curves. At this step, $\mathrm{DCF}_{ij}$ are binned by their associated time lag, $\tau_{ij} = t_i - t_j$ into equal width bins. The average of the bins yields the DCF($\tau$).

The normalisation (mean and standard deviation of respective light curves) used in the estimation of the DCF($\tau$) assumes that the light curves are statistically stationary. Under this assumption, the DCF sometimes can exceed unity (DCF($\tau$) $> 1$) making the interpretation difficult. A workaround for this problem is to estimate the mean and standard deviation only from the points that overlap at a given time lag bin (cf. White & Peterson 1994; Welsh 1999). Thus, with this local normalisation the resultant DCF is bound to the $[-1, +1]$ interval. A positive DCF($\tau$) implies a correlated variability and an anti-correlation when it is negative. The uncertainties of the DCF can be estimated by a model-independent Monte Carlo method (Peterson et al. 1998) that accounts for the effects of measurement noise and data sampling. This method consists of a bootstrap selection of a subsample of data points from each light curve to which Gaussian noise with a standard deviation matching the observational error bars is added. The time lags can be estimated from the peak of the cross-correlation or by

fitting a Gaussian function to the DCF peak. Alexander (2013) describes an algorithm, PLIKE, that estimates the maximum likelihood of the DCF points. According to this method, the maximum likelihood estimate coincides with the peak of the cross-correlation. The fiducial interval is then estimated by interpolating between the points of the likelihood function (see Alexander 2013).

## 3.3 Significance of the Correlation

The factors affecting the correlations are stochastic nature of the variability, data sampling and measurement errors. Also, the frequent appearance of flares means that high correlation coefficients between any two wavebands are to be expected even in the absence of any physical relation between the processes responsible for their production. Hence, the statistical significance of the DCF can be investigated by Monte Carlo simulations, in turn, estimating the probability if chance correlations primarily limit the observed correlation. The widely followed procedure to estimate the significance is by the cross-correlation of simulated light curves with power-law power spectral densities (PSD $\propto f^{-\alpha}$). In addition to this, two methods have been proposed recently by Fuhrmann et al. (2014), where the significance of the cross-correlation is quantified using mixed source correlations and stacking analysis.

### 3.3.1 Correlation of simulated light curves

The AGN light curves, in general, can be modelled by red-noise power spectra showing variability at all time scales, e.g. Hufnagel & Bregman (1992) in the radio and optical, Lawrence & Papadakis (1993) in the X-rays, and Abdo et al. (2010c) in $\gamma$ rays. Hence to construct the significance level of the cross-correlations, the following steps can be implemented:

(i) Simulate $N$ light curves using the algorithm by EMP13 for both the wavebands under study. Add Gaussian or Poisson noise to the simulated light curve depending on the frequency.

(ii) Cross-correlate every simulated light curve at one band with those at the other similar to the observed light curves as discussed in Section 3.2.

(iii) This yields a distribution of the cross-correlation coefficients for each

time lag bin. The significance level can then be estimated for each distribution based on Gaussian probability, such as 68.27 per cent ($1\sigma$), 95.45 per cent ($2\sigma$) and 99.73 per cent ($3\sigma$).

### 3.3.2 Mixed source correlations

The significance levels of the cross-correlation under this context is estimated by cross-correlating all sources with possible combinations from the source sample excluding the source under study. For example, a source list with ten sources can yield 81 cross-correlations by excluding the source of interest. The cross-correlations are performed similar to that described in Section 3.2. The significance levels can be estimated just as mentioned in step (iii) of Section 3.3.1. This approach of using every source in the sample instead of simulating light curves is done under the assumption that the flares exhibited by the source at different frequencies are physically unrelated. It is similar to the method where light curves are simulated over a range of PSDs under the assumption that all the sources exhibit similar variability properties, i.e. characterised by red-noise PSDs (e.g. Agudo et al. 2011a,b; Schinzel et al. 2011). This also assumes that the light curves are sampled in the same way, which is strictly not true in the case of radio and optical observations.

### 3.3.3 Stacking the correlations

Unless the variations at both wavebands under study correlate with a certain time lag, there will be no significant detection in the correlation. Hence, to improve the sensitivity for the detection of correlations, Fuhrmann et al. (2014) proposed the method of stacking or averaging the correlations obtained from the whole source sample. The stacking could also be performed on those light curves that have been normalised by dividing with the mean.

To estimate the significance of the stacked correlations, the mixed source correlations, discussed in Section 3.3.2, are more ideal than correlation of simulated light curves. In addition to estimating the time lag from the peak (observer's frame), one can always estimate the time lag in the source's frame by scaling the time values with a factor of $1/(1+z)$.

### 3.4 Bayesian Blocks

The Bayesian Block algorithm characterises the variability in time series data (Scargle et al. 2013). The algorithm finds and constrains the best partition of the observation interval into blocks, such that the source intensity is modelled as varying from one block to another, but constant within each block. Every block is the weighted mean estimate of the source intensity.

The location of the transitions between blocks is determined by optimising a fitness function for the partitions. In turn, it globally optimises the multiple change-point problems. In time series, a point at which a statistical model undergoes an abrupt transition, by one or more of its parameters jumping instantaneously to a new value, is called a "change point". To initiate the algorithm, one has to provide a prior value for the number of change points, ncp_prior, and also an estimate for the false positive rate[1], $p_0$.

The three fitness functions that can be used with the Bayesian blocks are discussed as follows. For more discussion on the topic and derivation of the equations, see Scargle et al. (2013).

(a) **Event Data:** This block fitness targets the times from discrete events where it associates every event with one data cell. Thus, for photon counting experiments, this block model is applicable as it partitions a block based on the arrival time of photons. The fitness function, in this case, is the logarithm of the maximum likelihood given in equation (3.8), where $N^{(k)}$ is the number of events in block $k$ and $T^{(k)}$ is the length of the block. The formula for ncp_prior given in equation (3.9) was obtained from the simulation of signal-free observational noise.

$$\log L_{\max}^{(k)} + N^{(k)} = N^{(k)}(\log N^{(k)} - \log T^{(k)}) \tag{3.8}$$

$$\text{ncp\_prior} = 4 - 73.53 p_0 N^{-0.478}. \tag{3.9}$$

(b) **Binned Event Data:** This fitness function is appropriate for an event detector accumulating counts over time. Unlike the above function, the counts bin can have arbitrary gaps. The block fitness function is given in equation (3.10), where $\lambda$ is the true event rate and $w^{(k)}$ is the sum of bin efficiencies in the block. The ncp_prior

[1]The probability of falsely reporting detection of a change point, similar to the value of alpha used in significance tests.

formula given in equation (3.11) was obtained for independently distributed events from a simulation study.

$$\log L^{(k)} = N^{(k)} \log \lambda - \lambda w^{(k)} \tag{3.10}$$

$$\text{ncp\_prior} = -\log(\gamma). \tag{3.11}$$

(c) **Point Measurements:** A common aspect of measuring a signal at a sequence of times is to characterise its time dependence. In such cases, corruption due to measurement errors result from problems with the observating instrument, weather issues, and others. Assuming the observational errors are distributed normally with zero mean and given variance, this block fitness will be applicable for observations in the radio and optical wavebands. The logarithm of the fitness function to maximise is given in equation (3.12), where $x_n$ and $\sigma_n$ are the signal and observational errors, respectively. The formula for ncp_prior given in equation (3.13) was obtained from simulations for normally distributed point measurements.

$$\begin{aligned} &\log L^{(k)}_{\max} = b_k^2/4a_k \\ &a_k = \frac{1}{2}\sum_n \frac{1}{\sigma_n^2} \\ &b_k = -\sum_n \frac{x_n}{\sigma_n^2} \end{aligned} \tag{3.12}$$

$$\text{ncp\_prior} = 1.32 + 0.577 \log_{10}(N). \tag{3.13}$$

Apart from using the ncp_prior formulae for the three cases discussed above, an iterative approach suggested by Scargle et al. (2013) can also be used. This method attempts to balance the dependence of the number of change points on the false positive threshold. The result will be more conservative due to the control over false positive rate.

Throughout this thesis, a false positive threshold of 1 per cent and the iterative method for the prior on the number of blocks was adopted. For the 37 GHz and 95 GHz radio and optical light curves, the *point measurements* fitness function was adopted. For the $\gamma$ rays, the fitness function *event data* was used, for which the arrival time of photons were extracted from a region of $0^\circ.5$ radius centred on the source's coordinates. We resorted to the fitness function of *binned event data* for cases when the Bayesian blocks computation using the arrival time of photons was computationally intensive.

# 4. Correlated variability in *Fermi* /LAT blazars

The high sensitivity and unprecedented detection in the $\gamma$ rays by *Fermi* /LAT along with its uniform time coverage has now made it possible to study the physics of blazar emission mechanisms in detail. This chapter discusses the results from the study of the correlated variability in bright *Fermi* /LAT blazars.

## 4.1 Radio/Gamma-ray Connection

The measure of time variability can be a useful probe in understanding various emission processes in blazars. With this motive in mind, the cross-correlation analysis was performed on 55 blazars in the $\gamma$ rays with the 37 GHz Metsähovi radio data in Publication II. The sources were chosen such that the 37 GHz mean flux density was above 1 Jy for the time period 2008.6–2013.6 that encompasses the first five years of *Fermi* /LAT observations.

### 4.1.1 Results from PSD analysis

To characterise the variability time-scale of the sources, PSD slopes at radio and $\gamma$ rays were estimated following the method discussed in Section 3.1. To take the noise processes into account properly, a long time series would be highly beneficial. Hence, for most of the sources, over 20 years of Metsähovi data was used for the PSD estimation at the radio frequency. By taking into account the goodness of fit obtained from Monte Carlo simulations (see Section 3.1), only those sources with probability (corresponds to the percentile of $\chi^2_{\rm dist}$ from simulation that exceeds the observed) higher than 0.05 were accepted. In turn, PSD slopes for 51 and 48 sources were obtained in radio and $\gamma$-ray frequencies, respectively. The PSD slopes for blazars are thought to be simple power-laws,

with slopes between $-1$ and $-2$ corresponding to *red noise* processes. In an astronomical time series this noise process reflects on the presence of large amplitude variations in longer rather than in short time-scales. In the frequency domain this shows that with any increase in frequency the PSD decreases. In our analysis, the average PSD slopes in radio and in $\gamma$ rays were 2.1 and 1.2, respectively. The accepted PSD slopes for all the sources at both wavebands are shown in Table 1 of Publication II. The results indicates that the long-term variability dominates the radio light curves, while in the $\gamma$ rays the short-term variations are more pronounced.

### 4.1.2 Cross-correlation results

In an attempt to search for correlated variability in radio and $\gamma$ rays, the cross-correlation was performed using the DCF with local normalisation. Since sampling of the light curves has a major influence on the DCF peak, the cross-correlation of radio was performed with weekly and monthly binned $\gamma$-ray light curves. In Section 3.2, two methods for estimating the significance of the correlations were discussed: simulating light curves (hereafter Method 1) and mixed source correlations (hereafter Method 2). The correlation results from the perspective of both these methods were inspected and can be summarised as follows:

(a) **Method 1:** The cross-correlation of weekly binned $\gamma$-ray and radio light curves yielded 23 and 10 sources at $2\sigma$ and $3\sigma$ levels, respectively. Using monthly binned light curves, 23 and 13 sources were found at a significance of $2\sigma$ and $3\sigma$ levels.

(b) **Method 2:** The number of sources significant at $2\sigma$ and $3\sigma$ levels were 38 and 6 for the weekly binned light curves. For the monthly binned, 30 and 6 sources were found at $2\sigma$ and $3\sigma$, respectively.

From the results discussed above, it is evident that the number of sources are not significantly different when it comes to sampling, but it does differ by using the two methods. Hence, to overcome this ambiguity, only those sources significant in both the methods were considered as correlated ones. Another constraint was set based on chance probability, such that at least one source would be significantly correlated by chance. Hence, this threshold was set at a $2.36\sigma$ level based on the total number of sources in the sample (i.e. 54/55 = 98.18 per cent). In the end, the number of significant correlations were brought down to 20 and 23 sources from

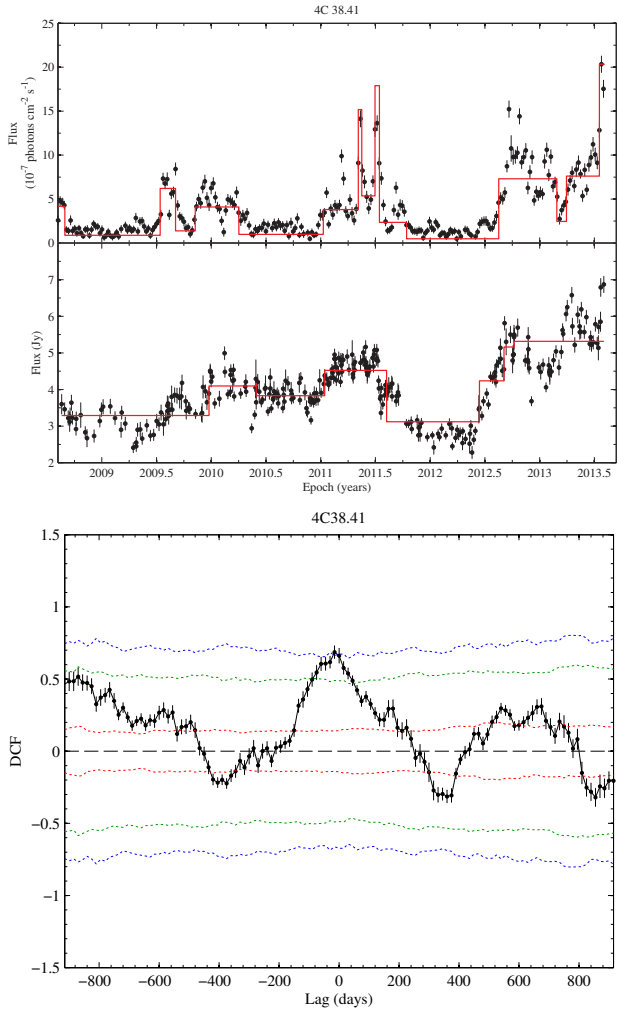


**Figure 4.1.** *Top:* Weekly-binned $\gamma$-ray (Top-panel) and radio (bottom-panel) light curves of the source 4C 38.41 from Publication II. Bayesian block representation is plotted in the red line over the light curve. *Bottom:* DCF of the light curves shown on top. The significance levels are plotted as red ($1\sigma$), green ($2\sigma$) and blue ($3\sigma$) dotted lines.

weekly and monthly binned light curves. The results are shown in Table 2 of Publication II. The time lags were in the range of $-850$–$690$ days, where a negative sign implies the emission in radio leading the $\gamma$ rays and vice versa for the positive sign. The radio/$\gamma$-ray light curve and the cross-correlation of the source 4C 38.41 is shown in Figure 4.1.

As mentioned in Section 3.3.3 to improve the sensitivity of detecting significant correlations, the stacking method was employed. All 55 sources were thus cross-correlated and averaged. The stacking was also made based on source class, i.e. FSRQs and BLOs. The significance of the stacked correlations were estimated with mixed source correlations. Hereagain, the stacking was done using both weekly and monthly binned $\gamma$-ray light curves. The results were 80 and 120 days, respectively. In the source frame, these results reduced to 47 and 70 days. All these results were significant at $3\sigma$ level.

### 4.1.3 Bayesian Blocks

To characterise the variability at both the radio and $\gamma$ rays, the Bayesian blocks algorithm (discussed in Section 3.4) was implemented. The algorithm partitions the light curves into blocks, each characterised by flux and duration. The radio and $\gamma$-ray light curve of the source 4C 38.41 along with the Bayesian blocks is shown in Figure 4.1. The variability of a source is represented by the number of blocks. Thus, through Figure 4.2, it can be understood that on average the correlated sources have more blocks, and thus are more variable than its uncorrelated counterpart.

## 4.2 Multifrequency Correlations

The search for correlated variability was extended in Publication III with the use of high-frequency radio (95 GHz CARMA observations) and $R$-band optical data alongside the Metsähovi 37 GHz and *Fermi*/LAT data. A total of 15 sources were selected for this work for the time period from 2012 August 1 to 2014 November 15.

### 4.2.1 Results from PSD analysis

The PSD slopes for the 95 GHz and $R$-band data were estimated following a similar approach implemented in Section 4.1.1. All 15 sources at 95 GHz

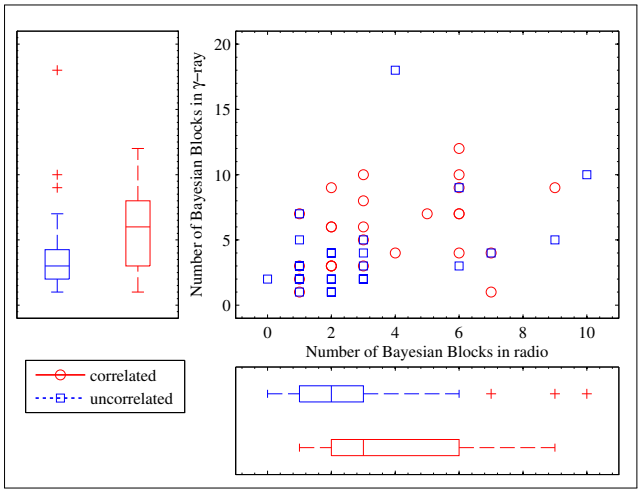


**Figure 4.2.** Scatter and boxplots for radio vs $\gamma$-ray for correlated and uncorrelated sources with number of Bayesian blocks from Publication II. The box comprises 75 per cent of the distribution of data with plus symbols denoting the outliers in the boxplots. The median of the distribution is denoted by a solid line in the box. The scaling of the boxplots are similar to the scatter plot.

and 9 sources in the $R$-band had acceptable PSD slopes with their respective probabilities higher than 0.05. The average PSD slopes at 95 GHz and $R$-band were 2.0 and 1.6, respectively. On comparison to those obtained at 37 GHz and $\gamma$-rays, the PSD slopes were found to decrease with increasing frequency. The PSD slopes at 95 GHz and $R$-band are given in Table 1 of Publication III.

### 4.2.2 Cross-correlation analysis

The light curves at four different wavebands were cross-correlated in a manner similar to the procedure used in Publication II. In the millimetre band (i.e. 37 and 95 GHz), eleven sources showed a significant correlation at a level of 99 per cent, and in optical and $\gamma$-ray correlation six sources were significant. All other correlations had less than five sources with significant correlation. The multifrequency light curve of 1510–089 along with all possible cross-correlations are shown in Figure 4.3.

## 4.3 Discussion

According to current theoretical models at distances $\gtrsim$1 pc, $\gamma$-ray emission is produced by an ICS mechanism with the seed photons arising either from external radiations that are dominated by the infrared thermal ra-

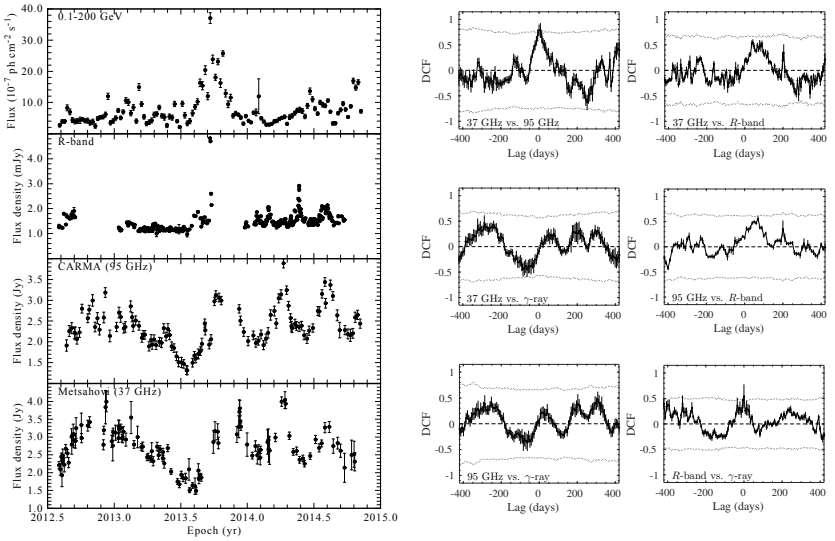


**Figure 4.3.** Multifrequency light curve of the source 1510-089 is shown on the left, with $\gamma$ rays to radio from top to bottom. The cross-correlations of the light curves are shown on the right. The grey dotted line in the DCF corresponds to a 99 per cent significance level. This is taken from Publication III.

diation emitted by the hot dust (Błażejowski et al. 2000) or from the relativistic jet producing the synchrotron radiation. Modelling the SED of the high-energy emission in FSRQs suggests the EIC dominance while those for BL Lacs favours the SSC mechanism (e.g. Abdo et al. 2010b; Böttcher et al. 2013). Recent observational evidence on 3C 454.3 by León-Tavares et al. (2013) shed light on the theory of outflowing BLR (see León-Tavares et al. 2011). According to this notion, the relativistic jet as it propagates downstream drags with it the BLR material serving as an alternative source of seed photons for the IC scattering. In such cases, the BLR emission-line variability can be powered by the non-thermal continuum emission of the jet.

Depending on the physics of the jet, the cross-frequency time delays from the DCF relate to the relative locations of the emission regions at different wavebands. The distance travelled by the emission region can be obtained from equation (4.1), where $\Delta t^{\rm obs}$ is the observed time delay

$$d = \frac{\beta_{\rm app} c \Delta t^{\rm obs}}{\sin\theta(1+z)} \tag{4.1}$$

In Publication II, the averaged estimate for the distance travelled from the radio/$\gamma$-ray connection was $\sim$7 pc in the observer's frame. From the averaged viewing angle and the redshift of the sample, the projected distance was $\sim$0.7 pc (0.08 mas). The average size of the radio core for the

sample in Publication II was $0.1\pm0.02$ mas, based on the multi-epoch VLBA observations reported in Jorstad et al. (2001a). These results suggest the $\gamma$-ray emission region to be co-spatial with the radio core. This causal connection is in agreement with the result obtained from the Bayesian blocks, which claims that the onset of the radio and $\gamma$-ray flares in most sources are quasi-simultaneous. This finding is similar to those reported in Lähteenmäki & Valtaoja (2003) and León-Tavares et al. (2011).

The time lags obtained from all cross-correlations in Publication III shows a frequency dependence with the time lags decreasing with increasing frequency. This is in agreement with synchrotron self-absorption effects, which is also described figuratively in Publication III and in Fuhrmann et al. (2014). The connection between various bands found in Publication III can be summarised as follows:

(a) **Millimetre connection:** The variations in the millimetre bands of most sources are simultaneous resulting in a near-zero time delay in cross-correlation analysis. According to opacity arguments in frequency dependent time lags, the emission at higher frequency leads those at lower frequency. However, the near-zero time delay obtained in most of the sources indicates that the opacity at 37 GHz and 95 GHz is similar.

(b) **Optical and $\gamma$-ray connection:** The time delay from the optical and $\gamma$-ray correlation show that the optical leads the $\gamma$ rays in one source, and the vice versa for three sources. A zero-time delay was obtained in two sources implying a co-spatialty of the two emission regions.

(c) **Millimetre and $\gamma$-ray connection:** In the millimetre and $\gamma$-ray cross-correlations very few sources showed significant correlation. Apart from the short time span of the light curves, the presence of an increasing/decreasing trend in the millimetre light curves are surmised to have greater impact on producing a statistically significant correlation. Also the absence of any major outburst in either bands in most sources can hamper the result.

(d) **Millimetre and optical connection:** Owing to the sparsely sampled optical data relative to those in the millimetre, and the presence of seasonal gaps in the optical light curves no tighter constraint can be placed on the physics of this connection. Although three sources showed a significant correlation in this analysis.

The time delays reported in Publications II and III can be approached from the perspective of shock-shock interaction, where the effects due to light-travel delays and frequency stratification play a major role. It was recently pointed out by Nalewajko et al. (2014), that the high-energy emission region cannot be constrained merely based on a temporal coincidence between the radio/$\gamma$-ray flares. The authors using the light-travel argument proposed that a $\Gamma > 50$ would be required to place the $\gamma$-ray emission region to the parsec-scale jet. This statement is valid only for long time delays and can be turned down based on the correspondence of the start time of both radio and $\gamma$-ray activity in Publication II.

From the fractional variability of the sources in Publications II and III, the $\gamma$ rays are considered to be more variable than light curves in other bands. The fractional variability is found to decrease with increasing time lags as discussed in Publication III. Thus, for luminous blazars a tighter constraint on the physics of the high-energy emission mechanism can be set from the time variability analysis. In general, for symmetric flares in optical with a lack of optical/radio correlation, the high-energy emission region can be situated closer to the black hole since the seed photon field from the torus is expected to be constant, unlike those photons from the shocked regions in the SSC model. In cases where the $\gamma$-ray emission is characterised by the optical synchrotron photons, the variability time-scale of the emission at both wavebands are expected to be the same. However, the PSD slopes of some sources are relatively flatter in the $\gamma$ rays compared to the optical. This could possibly imply a compact emission region within the jet or a turbulent jet flow (e.g. Ghisellini & Tavecchio 2008; Marscher 2014).

In Publication V the radio and $\gamma$-ray connection in the BLO Mrk 421 was studied. The $\gamma$-ray flare in 2012 and 2013 was modelled under a single-zone emission model. Under the one-zone SSC hypothesis, the 2013 $\gamma$-ray flare was considered to be produced from an instantaneous electron injection, while the width of the radio flare was related to the cooling time of the electrons. The radio flare in 2012 was associated with the double peaked $\gamma$-ray flare, and was reproduced with a varying Doppler factor in one case and an increased magnetic field strength in the other. Both the $\gamma$-ray flares in 2012 and 2013 preceded the radio ones by $\sim$60 days.

The radio to $\gamma$-ray behaviour of the FSRQ OJ 248 was studied in Publication VI. The correlated variability of the 2012 outburst across radio, optical, X-ray and $\gamma$-ray bands were studied. A significant correlation was

reported between all possible pairs of light curves, with the exception of 37 GHz that showed less pronounced outburst in 2012. A similar finding was obtained in Publication II. A co-spatial origin of the X-ray and millimetre emission was also suggested from the zero-time delay in cross-correlations.

The results in both Publications II and III shows that more than 50 per cent of the sources are uncorrelated. Apart from the sparse sampling, the possible reason is the so-called "orphan" activity, with the lack of emission in either the lower or higher frequency. The possible cause of a $\gamma$-ray activity with no radio counterpart has been attributed to the hadronic processes (Böttcher 2007). In the case of an orphan optical flare it is possibile that the evolution of shocks is disrupted due to radiative losses, in turn dissipating energy rapidly (Marscher & Gear 1985). Activity observed only in the radio frequencies could be due to the complex shock structure and shock interactions that are required for producing the high-energy activity (Aller et al. 2014). According to the Turbulent Extreme Multi-Zone model (Marscher 2014), orphan flares are due to the combined effects of the modulation in the magnetic field and electron energy distribution across different turbulent cells and light-travel delay.

# 5. Case study: 1156+295

The source 1156+295 is a FSRQ at redshift, $z$ = 0.729. It displays strong variability across the electromagnetic spectrum with an active phase in the $\gamma$ rays during the year 2010. Hence, to study the flaring behaviour and to determine the $\gamma$-ray emission region in the source, a multifrequency analysis was performed in Publication I. The data from radio through $\gamma$-rays were obtained from different observatories as detailed in Chapter 2. Apart from the single-dish radio observations, 43 GHz VLBA data was also used to study the kinematics of the jet.

The multifrequency light curve of the source is shown in Figure 5.1. The $\gamma$-ray light curve is characterised by a large intensity flare coupled with minor intensity variations for more than three months in 2010 before returning to a quiescent state. Flare B, with a peak flux of $1.4 \times 10^{-6}$ photons cm$^{-1}$ s$^{-1}$, is the brightest event observed in the $\gamma$-ray light curve. Another prominent activity was observed towards the end of 2011. The active phase in $\gamma$ rays was characterised with Bayesian blocks. The variability time-scales of the flares are in the range of 8–15 days. In the optical wavebands the source was flaring roughly on a yearly basis, but owing to the gaps due to solar conjuncture the data was not much useful to the analysis. At millimetre wavelengths the source exhibited two characteristic exponential flares.

The morphology of the blazar jet from 43 GHz VLBA observations reveal four moving (C1, C2, C3 and C4), and one stationary (S1), component (Figure 5.2). The moving components were modelled with a polynomial (first order for C1, C2, and C3; second order for C4), which yields the proper motion (slope of the fit) and the ejection epoch of the components (determined by back-extrapolating the fitted linear trajectory). The physical parameters – $\beta_{\rm app}$, $\delta$, $\Gamma$, and $\theta$ – of the moving components were estimated.

The cross-correlation of the VLBA core with the $\gamma$-ray light curve showed

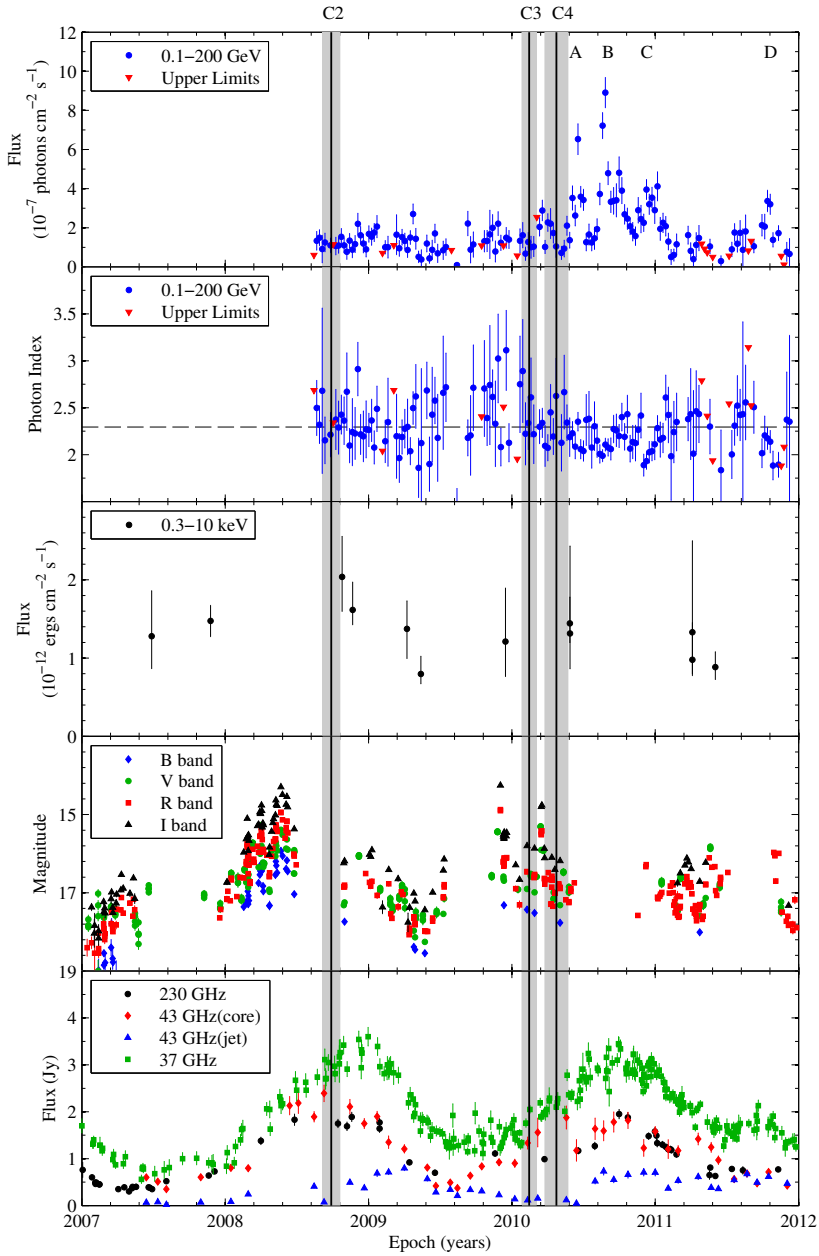


**Figure 5.1.** Multifrequency light curve of 1156+295 from 2007 through 2011 taken from Publication I. From the top: (1) weekly binned $\gamma$-ray flux from *Fermi* /LAT at 0.1–200 GeV; $2\sigma$ upper limits are denoted as inverted red triangles. (2) Photon Index of the weekly binned $\gamma$-ray light curve; the dashed line represents the 2FGL photon index estimate. (3) *Swift*/XRT X-ray flux at 0.3–10 keV. (4) Optical data at various bands. The gaps in the optical data are due to solar conjuncture. (5) Variations at millimetre wavelengths in the bottom panel. The vertical lines are the ejection epochs of the components C2 (2008.74), C3 (2010.12) and C4 (2010.31) obtained from the VLBA data with their $1\sigma$ uncertainties denoted by the corresponding shaded interval.

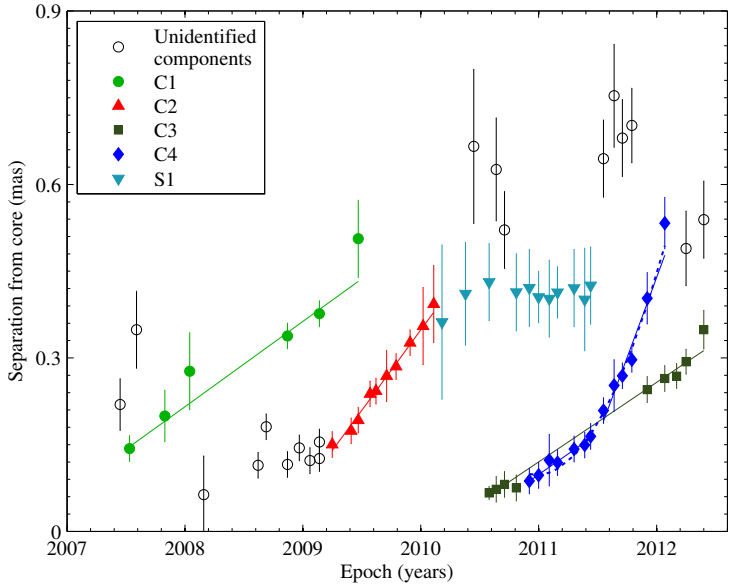


**Figure 5.2.** Component separation from the 43 GHz radio core versus time in 1156+295. Four moving components (C1, C2, C3, and C4) and one stationary component (S1) are identified in the jet. The solid lines indicate motion with no acceleration while the dotted lines indicate accelerated motion fits. This plot is taken from Publication I.

a peak at $-120$ days with the core leading the $\gamma$-ray at a $2\sigma$ significance level. The result had to be handled with caution since the DCF peak was broad with the peak also extending to the positive time lag. The cross-correlation of the 37 GHz light curve with the monthly binned $\gamma$-ray in Publication II resulted in the radio emission lagging the $\gamma$ rays by 25 days. The DCF peak obtained, in this case, had a confidence interval of [11, 92] days. Therefore, on comparing the cross-correlation results in Publications I and II, the variability at radio and $\gamma$ rays can be understood to have different time-scales: a year-long activity period in the radio while variability on daily or weekly time-scales in $\gamma$ rays.

The disparity of the two results discussed above could imply superposition of multiple events in the radio light curves. The radio peak remains at $\sim$3 Jy for more than five months before it starts to decay. A similar trait is also seen from the VLBA radio core flux around the same time, however, with two distinct flux maxima in 2010. This can be tied to the ejection of components C3 and C4. The ejection epoch of these components correspond to the beginning of strong $\gamma$-ray activity (see Figure 5.1).

Based on the theory of moving shocks (discussed in section 1.3) C4 can be classified as a trailing shock forming in the wake of the leading com-

ponent, C3. According to the simulation of Agudo et al. (2001), trailing shocks represent pinch waves excited by the main disturbance, which pervades the expanding jet accelerating to superluminal speeds. In line with the last statement, C4 after propagating over $\sim$0.2 mas accelerates, increasing its apparent speed to 23.2$c$ (Figure 5.2). The split of C4 from C3 toward the end of 2010 coincides with the $\gamma$-ray flare C.

The flux density evolution of C4 shows considerable variability that could be due to the interaction with S1 (formed by early 2010) at about 0.4 mas around 2011.5. The time of this interaction coincides with the sub-flare D in the $\gamma$ rays, which constrains the emission region of this sub-flare $\gtrsim$4 pc (projected) from the radio core. These results are in favour of the far-dissipation scenario, where SSC is the dominant $\gamma$-ray emission mechanism.

From the morphology of the jet and other results discussed above it is clear that the physics of the jet during the $\gamma$-ray high state is far more complex. To understand the evolution of the shocks during this period, the radio spectra of 1156+295 obtained in Publication IV are analysed (see Figure 5.3). The spectra were obtained as part of the *Planck* campaign with observations at four different epochs spanning the 2010 radio flare: first two observations were during the rising phase of the radio flux and the rest during their decay. The spectra were modelled using a broken power-law of the form:

$$S_\nu \propto \begin{cases} \nu^{\alpha_{\rm mm}} & \text{for } \nu \leq \nu_{\rm break} \\ \nu_{\rm break}^{(\alpha_{\rm mm}-\alpha_{\rm sub-mm})}\, \nu^{\alpha_{\rm sub-mm}} & \text{for } \nu > \nu_{\rm break} \end{cases} \tag{5.1}$$

where $\alpha_{\rm mm}$ and $\alpha_{\rm sub-mm}$ are the spectral indices for the millimetre and sub-millimetre part of the spectrum, and $\nu_{\rm break}$ is the break frequency. The evolution of the spectra in most sources in Publication IV seems to behave according to the predictions of the shock-in-jet model: the flux density increases with any decrease in break frequency in the first stage (Compton losses), followed by a constant flux density phase with decreasing break frequency (synchrotron losses), and, finally, both flux density and the break frequency decreases (adiabatic losses). In this source, the break frequency shifts from 44 GHz in the first spectra to 24 GHz in the final spectra. However, it is evident from Figure 5.3 that the flux density never reaches a plateau phase with the decrease in the break frequency. This suggests the lack of synchrotron losses during the evolution of the 2010 radio flare. Similar results have been reported in 3C 345 (Lobanov

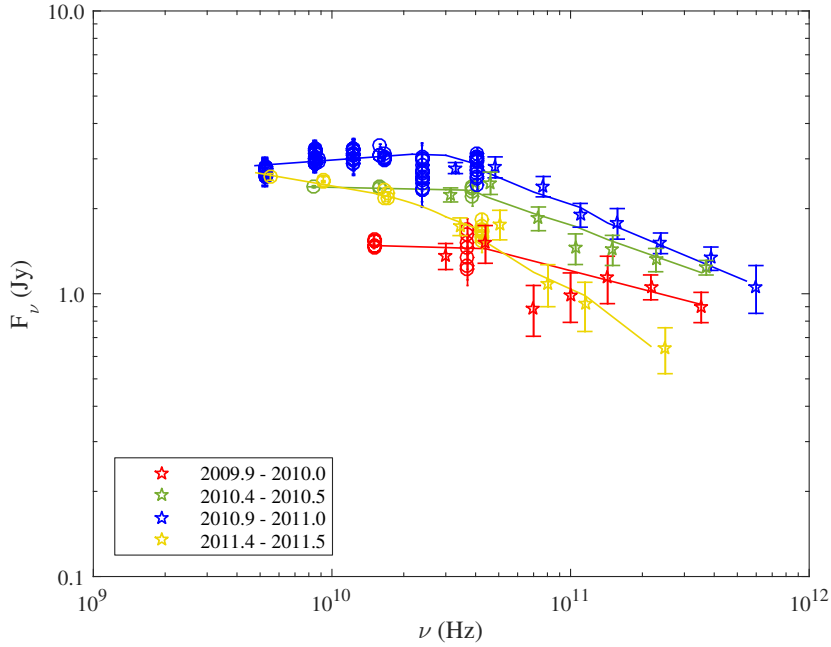


**Figure 5.3.** Radio spectra of 1156+295 during *Planck* observations. All *Planck* data are shown with a star symbol while other radio data as open circles. Data other than those in red are shifted in frequency by five per cent for clarity with the points and error bars. This plot is from Publication IV.

& Zensus 1999) and CTA 102 (Fromm et al. 2011).

The shape of all spectra in Figure 5.3 appears to be smooth, except the first spectrum that displays a complex structure. Two distinct humps are visible in the first spectrum, which could characterise the presence of multiple shocks in the jet. This is in agreement with the finding of two components from the VLBA analysis.

# 6. Conclusions

The uniform all-sky coverage of *Fermi* has been exploited through a detailed study of the blazar 1156+295, and a systematic search for multifrequency correlations for a sample of FSRQs and BLOs. The results in Publication I showed how the evolution of shocks and shock-shock interaction played a dominant role in the production of $\gamma$-ray flares. In Publication II, the correlated variability in sources along with the size of the radio core showed evidence for the $\gamma$-ray emission to be co-spatial with the radio core. This evidence for the parsec-scale $\gamma$-ray emission, however, challenges the observed variability time-scales that are of the order of weeks at $\gamma$ rays, under a one-zone framework. A workaround to this problem is to assume multiple smaller zones that show rapid variability. Different realisations of this model are discussed in the literature, such as the pipe geometry model by Graff et al. (2008), Monte Carlo radiative transfer models including the Fokker-Planck equations by Chen et al. (2011), magnetic reconnection by Giannios (2013) and the turbulence scenario by Marscher (2014). On the same note, the SED model for FSRQs has to be revisited since the dominance of the SSC component for the $\gamma$-ray emission is shown to be much higher in these works.

The importance of well-sampled data can be understood from the lack of significant results in Publication III. Only with such data, will it be possible to take the noise properties of the light curves properly into account for most variability studies. In addition to this, long-term monitoring campaigns are to be performed to understand the evolution of flares over different activity periods. Also from the perspective of correlations, the chances of obtaining significant correlations for long time series are higher since the activity cycle of flares are on average six years (Hovatta et al. 2007). The near-zero time delay obtained in the millimetre correlation analysis of Publication III shows the importance of 37 GHz light

curves, since continued monitoring of sources at higher frequencies such as 95 GHz, in this case, are seldom possible.

Thus, through this thesis, the importance of variability in relativistic jets and its connection across the electromagnetic spectrum can be stressed. However, to understand the mechanisms such as the jet launching, acceleration and collimation, among others, one has to probe the shocked regions of the jet at much higher resolution, usually with the aid of VLBI observations. Therefore, the necessity for continued monitoring of AGN using VLBI in the future is stressed. The simultaneous radio spectra obtained during the *Planck* campaign has shown that the spectral shapes of most of the sources are in agreement with the shock-in-jet model. A better understanding of the radiative processes in the shocks requires physical modelling of the radio spectra. Polarisation and spectral analysis for a sample of sources will serve as a useful tool in understanding the magnetic field and energy density of relativistic electrons. These results will, therefore, tie loose ends with the SED modelling, and thus will be able to set more stringent limits on the physics of the blazar zone.

# References


Abdo A. A., et al., 2010a, ApJS, 188, 405

Abdo A. A., et al., 2010b, ApJ, 716, 30

Abdo A. A., et al., 2010c, ApJ, 722, 520

Ackermann M., et al., 2012, ApJS, 203, 4

Agudo I., Gómez J.-L., Martí J.-M., Ibáñez J.-M., Marscher A. P., Alberdi A., Aloy M.-A., Hardee P. E., 2001, ApJ, 549, L183

Agudo I., et al., 2011a, ApJ, 726, L13

Agudo I., et al., 2011b, ApJ, 735, L10

Agudo I., Gómez J. L., Casadio C., Cawthorne T. V., Roca-Sogorb M., 2012, ApJ, 752, 92

Alexander T., 2013, preprint, (arXiv:1302.1508)

Aller M. F., Hughes P. A., Aller H. D., Latimer G. E., Hovatta T., 2014, ApJ, 791, 53

Aloy M.-Á., Martí J.-M., Gómez J.-L., Agudo I., Müller E., Ibáñez J.-M., 2003, ApJ, 585, L109

Antonucci R., 1993, ARA&A, 31, 473

Atwood W. B., et al., 2009, ApJ, 697, 1071

Balick B., Brown R. L., 1974, ApJ, 194, 265

Belloni T., ed. 2010, The Jet Paradigm Lecture Notes in Physics, Berlin Springer Verlag Vol. 794

Biretta J. A., Zhou F., Owen F. N., 1995, ApJ, 447, 582

Björnsson C.-I., 2010, ApJ, 723, 417

Blandford R. D., Königl A., 1979, ApJ, 232, 34

Blandford R. D., Znajek R. L., 1977, MNRAS, 179, 433

Błażejowski M., Sikora M., Moderski R., Madejski G. M., 2000, ApJ, 545, 107

Bloom S. D., 2008, AJ, 136, 1533

Bloom S. D., Marscher A. P., 1996, ApJ, 461, 657

Böttcher M., 2007, Ap&SS, 309, 95

Böttcher M., Reimer A., Sweeney K., Prakash A., 2013, ApJ, 768, 54

Brown R. L., Lo K. Y., 1982, ApJ, 253, 108

Cash W., 1979, ApJ, 228, 939

Chen X., Fossati G., Liang E. P., Böttcher M., 2011, MNRAS, 416, 2368

Cheung C. C., Harris D. E., Stawarz Ł., 2007, ApJ, 663, L65

Cohen M. H., et al., 2014a, ApJ, 787, 151

Cohen D. P., Romani R. W., Filippenko A. V., Cenko S. B., Lott B., Zheng W., Li W., 2014b, ApJ, 797, 137

Curtis H. D., 1918, Publications of Lick Observatory, 13, 9

Daly R. A., Marscher A. P., 1988, ApJ, 334, 539

della Ceca R., Lamorani G., Maccacaro T., Wolter A., Griffiths R., Stocke J. T., Setti G., 1994, ApJ, 430, 533

Dermer C. D., Schlickeiser R., Mastichiadis A., 1992, A&A, 256, L27

Drake A. J., et al., 2009, ApJ, 696, 870

Edelson R. A., Krolik J. H., 1988, ApJ, 333, 646

Elvis M., et al., 1994, ApJS, 95, 1

Emmanoulopoulos D., McHardy I. M., Papadakis I. E., 2013, MNRAS, 433, 907

Errando M., et al., 2008, in Aharonian F. A., Hofmann W., Rieger F., eds, American Institute of Physics Conference Series Vol. 1085, American Institute of Physics Conference Series. p. 423

Fath E. A., 1909, Lick Observatory Bulletin, 5, 71

Fromm C. M., et al., 2011, A&A, 531, A95

Fugmann W., 1988, A&A, 205, 86

Fuhrmann L., et al., 2014, MNRAS, 441, 1899

Gaskell C. M., Peterson B. M., 1987, ApJS, 65, 1

Ghisellini G., Tavecchio F., 2008, MNRAS, 386, L28

Giannios D., 2013, MNRAS, 431, 355

Giommi P., et al., 2012, A&A, 541, A160

Graff P. B., Georganopoulos M., Perlman E. S., Kazanas D., 2008, ApJ, 689, 68

Greenstein J. L., 1963, Nature, 197, 1041

Hartman R. C., et al., 1999, ApJS, 123, 79

Hovatta T., Tornikoski M., Lainela M., Lehto H. J., Valtaoja E., Torniainen I., Aller M. F., Aller H. D., 2007, A&A, 469, 899

Hovatta T., Valtaoja E., Tornikoski M., Lähteenmäki A., 2009, A&A, 494, 527

Hubble E. P., 1926, ApJ, 64, 321

Hufnagel B. R., Bregman J. N., 1992, ApJ, 386, 473

Hughes P. A., Aller H. D., Aller M. F., 1985, ApJ, 298, 301

Hughes P. A., Aller H. D., Aller M. F., 1989, ApJ, 341, 54

Jansky K. G., 1933, Nature, 132, 66

Jorstad S. G., Marscher A. P., Mattox J. R., Wehrle A. E., Bloom S. D., Yurchenko A. V., 2001a, ApJS, 134, 181

Jorstad S. G., Marscher A. P., Mattox J. R., Aller M. F., Aller H. D., Wehrle A. E., Bloom S. D., 2001b, ApJ, 556, 738

Jorstad S. G., et al., 2005, AJ, 130, 1418

Jorstad S. G., et al., 2010, ApJ, 715, 362

Kadler M., Ros E., Lobanov A. P., Falcke H., Zensus J. A., 2004, A&A, 426, 481

Kovalev Y. Y., Lobanov A. P., Pushkarev A. B., Zensus J. A., 2008, A&A, 483, 759

Kovalev Y. Y., et al., 2009, ApJ, 696, L17

Lähteenmäki A., Valtaoja E., 1999, ApJ, 521, 493

Lähteenmäki A., Valtaoja E., 2003, ApJ, 590, 95

Lawrence A., Papadakis I., 1993, ApJ, 414, L85

Lea S. M., Mushotzky R., Holt S. S., 1982, ApJ, 262, 24

León-Tavares J., Lobanov A. P., Chavushyan V. H., Arshakian T. G., Doroshenko V. T., Sergeev S. G., Efimov Y. S., Nazarov S. V., 2010, ApJ, 715, 355

León-Tavares J., Valtaoja E., Tornikoski M., Lähteenmäki A., Nieppola E., 2011, A&A, 532, A146

León-Tavares J., et al., 2013, ApJ, 763, L36

Lister M. L., Homan D. C., Kadler M., Kellermann K. I., Kovalev Y. Y., Ros E., Savolainen T., Zensus J. A., 2009, ApJ, 696, L22

Lister M. L., et al., 2013, AJ, 146, 120

Lobanov A. P., 1998, A&A, 330, 79

Lobanov A. P., Zensus J. A., 1999, ApJ, 521, 509

Lovell J., 2000, in Hirabayashi H., Edwards P. G., Murphy D. W., eds, Astrophysical Phenomena Revealed by Space VLBI. p. 301

Maraschi L., Ghisellini G., Celotti A., 1992, ApJ, 397, L5

Marscher A. P., 1995, Proceedings of the National Academy of Science, 92, 11439

Marscher A. P., 2005, Mem. Soc. Astron. Italiana, 76, 13

Marscher A. P., 2014, ApJ, 780, 87

Marscher A. P., Gear W. K., 1985, ApJ, 298, 114

Mattox J. R., et al., 1996, ApJ, 461, 396

Max-Moerbeck W., et al., 2014a, MNRAS, 445, 428

Max-Moerbeck W., Richards J. L., Hovatta T., Pavlidou V., Pearson T. J., Readhead A. C. S., 2014b, MNRAS, 445, 437

Minkowski R., 1960, ApJ, 132, 908

Miyamoto S., Kimura K., Kitamoto S., Dotani T., Ebisawa K., 1991, ApJ, 383, 784

Muecke A., et al., 1997, A&A, 320, 33

Nalewajko K., Begelman M. C., Sikora M., 2014, ApJ, 789, 161

Nieppola E., Tornikoski M., Valtaoja E., 2006, A&A, 445, 441

Nieppola E., Tornikoski M., Valtaoja E., León-Tavares J., Hovatta T., Lähteenmäki A., Tammi J., 2011, A&A, 535, A69

Nolan P. L., et al., 2012, ApJS, 199, 31

O'Sullivan S. P., Gabuzda D. C., 2009, MNRAS, 400, 26

Oppenheim A. V., Schafer R. W., 1975, Digital signal processing. Englewood Cliffs: Prentice-Hall

Padovani P., Giommi P., 1995, ApJ, 444, 567

Papadakis I. E., Lawrence A., 1993, MNRAS, 261, 612

Pearson T. J., Zensus J. A., 1987, in Zensus J. A., Pearson T. J., eds, Superluminal Radio Sources. p. 1

Peterson B. M., 2008, New A Rev., 52, 240

Peterson B. M., Wanders I., Horne K., Collier S., Alexander T., Kaspi S., Maoz D., 1998, PASP, 110, 660

Press W. H., Teukolsky S. A., Vetterling W. T., Flannery B. P., 1992, Numerical recipes in FORTRAN. The art of scientific computing. Cambridge: University Press, |c1992, 2nd ed.

Pushkarev A. B., Hovatta T., Kovalev Y. Y., Lister M. L., Lobanov A. P., Savolainen T., Zensus J. A., 2012, A&A, 545, A113

Rastorgueva E. A., Wiik K. J., Bajkova A. T., Valtaoja E., Takalo L. O., Vetukhnovskaya Y. N., Mahmud M., 2011, A&A, 529, A2

Reber G., 1944, ApJ, 100, 279

Rees M. J., 1966, Nature, 211, 468

Rolke W. A., López A. M., Conrad J., 2005, Nuclear Instruments and Methods in Physics Research A, 551, 493

Rybicki G. B., Lightman A. P., 1979, Radiative processes in astrophysics. New York, Wiley-Interscience

Sault R. J., Teuben P. J., Wright M. C. H., 1995, in Shaw R. A., Payne H. E., Hayes J. J. E., eds, Astronomical Society of the Pacific Conference Series Vol. 77, Astronomical Data Analysis Software and Systems IV. p. 433

Scargle J. D., Norris J. P., Jackson B., Chiang J., 2013, ApJ, 764, 167

Schinzel F. K., et al., 2011, A&A, 532, A150

Schmidt M., 1963, Nature, 197, 1040

Schreiber T., Schmitz A., 1996, Physical Review Letters, 77, 635

Seyfert C. K., 1943, ApJ, 97, 28

Shen Y., Liu X., Greene J. E., Strauss M. A., 2011, ApJ, 735, 48

Shepherd M. C., 1997, in Hunt G., Payne H., eds, Astronomical Society of the Pacific Conference Series Vol. 125, Astronomical Data Analysis Software and Systems VI. p. 77

Sikora M., Begelman M. C., Rees M. J., 1994, ApJ, 421, 153

Slipher V. M., 1917, Lowell Observatory Bulletin, 3, 59

Smith F. G., 1951, Nature, 168, 555

Stocke J. T., Liebert J., Schmidt G., Gioia I. M., Maccacaro T., Schild R. E., Maccagni D., Arp H. C., 1985, ApJ, 298, 619

Teräsranta H., et al., 1998, A&AS, 132, 305

Timmer J., Koenig M., 1995, A&A, 300, 707

Urry C. M., Padovani P., 1995, PASP, 107, 803

Uttley P., McHardy I. M., Papadakis I. E., 2002, MNRAS, 332, 231

Valtaoja E., Teräsranta H., 1995, A&A, 297, L13

Valtaoja E., Teräsranta H., Urpo S., Nesterov N. S., Lainela M., Valtonen M., 1992a, A&A, 254, 71

Valtaoja E., Teräsranta H., Urpo S., Nesterov N. S., Lainela M., Valtonen M., 1992b, A&A, 254, 80

van der Klis M., 1997, in Babu G. J., Feigelson E. D., eds, Statistical Challenges in Modern Astronomy II. p. 321

Vaughan S., 2005, A&A, 431, 391

Vaughan S., Edelson R., Warwick R. S., Uttley P., 2003, MNRAS, 345, 1271

Welsh W. F., 1999, PASP, 111, 1347

White R. J., Peterson B. M., 1994, PASP, 106, 879

Williamson K. E., et al., 2014, ApJ, 789, 135

Wills B. J., Wills D., Breger M., Antonucci R. R. J., Barvainis R., 1992, ApJ, 398, 454

Blazars are active galaxies with jets oriented towards the line of sight of the observer. The emission from blazars is highly variable from radio through gamma-ray bands making them some of the most luminous objects in the Universe. Despite our current understanding, the physics regarding the formation and evolution of the jet - their morphology among others - remains unknown. Hence, it is important to study these objects across the electromagnetic spectrum and monitor them to assess their evolution. In this work, the widely debated issue of the emission region and mechanism of gamma rays in blazars is discussed. The total flux density curves at radio and optical bands, and photon fluxes at gamma rays are investigated using modified versions of power spectral density and cross-correlation analysis.

Aalto-DD 47/2016

ISBN 978-952-60-6704-9 (printed)
ISBN 978-952-60-6705-6 (pdf)
ISSN-L 1799-4934
ISSN 1799-4934 (printed)
ISSN 1799-4942 (pdf)

**Aalto University**
**School of Electrical Engineering**
**Metsähovi Radio Observatory**
**www.aalto.fi**

BUSINESS + ECONOMY

ART + DESIGN + ARCHITECTURE

SCIENCE + TECHNOLOGY

CROSSOVER

**DOCTORAL DISSERTATIONS**